

# Quantum Process Tomography of a Room-Temperature Alkali-Metal Vapor

Yujie Sun

*Marian Smoluchowski Institute of Physics, Jagiellonian University in Kraków, 30-348 Kraków, Poland*

Marek Kopciuch\*

*Institute of Spintronics and Quantum Information, Faculty of Physics, Adam Mickiewicz University, 61-614 Poznań, Poland and*

*Marian Smoluchowski Institute of Physics, Jagiellonian University in Kraków, 30-348 Kraków, Poland*

Arash Dezhang Fard

*Marian Smoluchowski Institute of Physics, Jagiellonian University in Kraków, 30-348 Kraków, Poland and Doctoral School of Exact and Natural Sciences, Jagiellonian University in Kraków, 30-348 Kraków, Poland*

Szymon Pustelny†

*Marian Smoluchowski Institute of Physics, Jagiellonian University in Kraków, 30-348 Kraków, Poland and Department of Physics, Harvard University, Cambridge, MA 02138, USA*

(Dated: August 28, 2025)

Quantum process tomography (QPT) is a technique for reconstructing the dynamics of open quantum systems under the Born-Markov approximation, as described by a Liouvillian superoperator, capturing both coherent and dissipative processes. While QPT is well established for qubits, it presents significant experimental challenges in multi-level qudits. In room-temperature atomic vapors, these difficulties arise from complex interactions, residual fields present in the system, environmental noise, and inhomogeneities in the medium. Overcoming these limitations is essential for accurate modeling and precise control of such systems—a critical step toward practical usage of the QPT. We present a QPT method that we experimentally validate on a room-temperature  $^{87}\text{Rb}$  vapor ensemble, achieving high-fidelity reconstruction of qutrit Liouvillians. Our approach establishes a computationally efficient framework for characterizing open quantum systems, enabling the study of non-unitary dynamics, efficient benchmarking of quantum sensors, and data-driven identification of environmental noise correlations.

## I. INTRODUCTION

Ranging from quantum sensing [1, 2] to quantum computation [3], the precise characterization of quantum processes is of crucial importance to realize the full potential of quantum technologies [4, 5]. In this context, it is important to note that many of the most versatile and accessible quantum platforms, including neutral atoms [6–9], trapped ions [10–12], color centers in diamond [13], linear optics [14–16], and superconducting circuits [17, 18], are inherently open systems whose dynamics involve an interplay between coherent evolution and complex environmental interactions. Moreover, extending quantum control beyond two-level systems (qubits) to multi-level systems (qudits) [19, 20] (e.g., qutrits [21]), which offer operations within larger Hilbert spaces and hence opening avenues for enhanced quantum protocols, faces a major challenge in obtaining full information about the evolution of these higher-dimensional systems in realistic, ambient settings where environmental decoherence and control imperfections strongly influence system evolution.

Quantum Process Tomography (QPT) [22–24] is a

technique that enables the reconstruction of the Liouvillian superoperator [25], capturing both coherent and dissipative dynamics [26]. While QPT is well established for qubits, it presents significant experimental challenges in multi-level systems (qudits). In particular, in room-temperature atomic vapors [27, 28], such difficulties stem from complex interactions, principally linear Zeeman splitting of the ground-state energy sublevels (degeneracy of level splittings), environmental noise, and inhomogeneous characteristics of the medium. Addressing these limitations is essential for accurate modeling and precise control of these systems, which is a critical step toward realizing practical and scalable quantum technologies based on these platforms.

The evolution of open quantum systems is most commonly described by the Lindblad master equation [29, 30], which (under the Born-Markov approximation [31–34]) provides a first-principles framework for modeling dynamics in QPT experiments. A standard reconstruction workflow proceeds as follows: (i) measurement of the system state at several discrete times, (ii) numerical integration of the master equation with a trial Liouvillian to generate theoretical trajectories, and (iii) iterative updating of the Liouvillian to minimize the discrepancy between simulation and experiment [18]. Although conceptually straightforward, this conventional reconstruction faces significant experimental and computational challenges. First, standard reconstruction

\* marek.kopciuch@amu.edu.pl

† szymon.pustelny@uj.edu.pl

methods require iterative numerical integration of Liouvillian operators, which often becomes intractable for large Hilbert spaces. Second, the formalism generally assumes a time-independent generator, thereby preventing the reconstruction of genuinely time-dependent Liouvillians that often govern realistic quantum dynamics. To overcome the time-independent limitation, recently, protocols based on machine learning [35] and continuous weak measurements [36] have been employed to reconstruct time-dependent Hamiltonians, and a protocol called quantum Liouvillian tomography [37] can even be used to characterize non-Markovian dynamics, including negative dissipation rates and time-dependent jump operators.

In this work, we investigate the Liouvillian of an effectively three-level system in the generalized Pauli basis, yielding a linear Bloch-Fano representation that analytically encodes system-environment couplings. This formulation produces closed-form solutions, removing the need for costly numerical integrations during optimization, and naturally extends to time-dependent Liouvillians, thereby revealing the temporal structure of the ensemble's environment. We experimentally validate our method on a  $F = 1$  hyperfine ground state of room-temperature  $^{87}\text{Rb}$  vapor ensemble, achieving high-fidelity reconstruction of qutrit Liouvillians, and demonstrate its scalability to higher-dimensional qudit systems.

The paper is organized as follows. Section II provides the theoretical framework and experimental platform underlying our QPT protocol. In Sec. III, we demonstrate the method in three representative scenarios: (i) evolution governed by relaxation, (ii) coherent dynamics under a static Hamiltonian, and (iii) dynamics under a time-dependent Hamiltonian. In each case, we present the reconstructed Liouvillians and assess their fidelity using the Frobenius norm. Two complementary data-analysis pipelines are compared to enforce physical constraints and quantify experimental uncertainty. The section concludes with a multiparameter reconstruction of time-dependent magnetic fields along three orthogonal axes. Finally, Sec. IV summarizes the main findings and outlines future research directions, while the Appendices and Supplementary Information provide additional theoretical derivations and experimental details.

## II. PRINCIPLES OF QUANTUM PROCESS TOMOGRAPHY

### A. Theoretical background

The dynamics of an open quantum system under the Born-Markov approximation [31, 32] are commonly described by the quantum master equation in the Lindblad

form:

$$\begin{aligned} \frac{d}{dt}\hat{\rho}(t) &= \hat{\mathcal{L}}[\hat{\rho}](t) \\ &= -i[\hat{H}, \hat{\rho}(t)] - \sum_{\mu} \left( \frac{1}{2} \{ \hat{L}_{\mu}^{\dagger} \hat{L}_{\mu}, \hat{\rho}(t) \} - \hat{L}_{\mu} \hat{\rho}(t) \hat{L}_{\mu}^{\dagger} \right), \end{aligned} \quad (1)$$

where  $\hat{\rho}(t)$  is the system density operator,  $\hat{H}$  is the system Hamiltonian,  $\hat{L}_{\mu}$  are the Lindblad quantum-jump operators representing dissipation channels indexed by  $\mu$ , and  $\hat{\mathcal{L}}$  is the corresponding Liouvillian superoperator. Here,  $[\cdot, \cdot]$  and  $\{\cdot, \cdot\}$  denote the commutator and anticommutator, respectively. Quantum operators are marked with a single hat, and superoperators acting on operators are denoted by a double hat.

Because  $\hat{\mathcal{L}}$  is a linear and trace-preserving superoperator on operators, it admits a matrix representation once operators are vectorized. Vectorization reshapes the density operator  $\hat{\rho}(t)$  into a vector  $|\rho(t)\rangle\rangle$  in a  $d^2$ -dimensional space, where  $d = \dim(\mathcal{H})$  is the Hilbert space dimension of the system. Correspondingly,  $\hat{\mathcal{L}}$  becomes a  $d^2 \times d^2$  matrix acting on  $|\rho(t)\rangle\rangle$ .

A convenient vectorization scheme employs the Bloch-Fano representation [38, 39], expanding operators in a basis of generalized Pauli matrices (see Appendix A). In this representation, the master equation (1) takes the form

$$\frac{d}{dt} |\rho(t)\rangle\rangle = \hat{\mathcal{L}}(t) |\rho(t)\rangle\rangle, \quad (2)$$

where the Liouvillian superoperator  $\hat{\mathcal{L}}(t)$  is allowed to depend explicitly on time. The formal solution to this equation is given by the time-ordered exponential

$$|\rho(t)\rangle\rangle = \mathcal{T} \exp \left( \int_0^t dt' \hat{\mathcal{L}}(t') \right) |\rho(0)\rangle\rangle \equiv \hat{P}(t) |\rho(0)\rangle\rangle, \quad (3)$$

where  $\mathcal{T}$  denotes time-ordering, which is necessary because  $\hat{\mathcal{L}}(t)$  at different times may not commute.  $\hat{P}(t)$  is the evolution superoperator, also called the process matrix, mapping the initial state vector  $|\rho(0)\rangle\rangle$  to  $|\rho(t)\rangle\rangle$ .

Our QPT protocol aims to reconstruct the evolution superoperator  $\hat{P}(t)$ , which fully characterizes the system dynamics. Following the method described in Refs. [40, 41], this reconstruction proceeds by preparing a set of initial states

$$M^{(i)} = \left\{ \left| \rho_k^{(i)} \right\rangle\rangle \text{ for } k = 1, \dots, N \right\}, \quad (4)$$

where  $N$  denotes the total number of prepared states. We then measure the outputs of these states after evolution under  $\hat{P}(t)$ :

$$\left| \rho_k^{(o)} \right\rangle\rangle = \hat{P}(t) \left| \rho_k^{(i)} \right\rangle\rangle. \quad (5)$$

Because each  $|\rho_k^{(i)}\rangle\rangle$  is a vector, Eq. (5) naturally generalizes to the matrix equation

$$\mathbb{M}^{(o)} = \hat{P}(t)\mathbb{M}^{(i)}, \quad (6)$$

where the input- and output-state matrices are defined as

$$\begin{aligned} \mathbb{M}^{(i)} &= \left( |\rho_1^{(i)}\rangle\rangle, \dots, |\rho_N^{(i)}\rangle\rangle \right), \\ \mathbb{M}^{(o)} &= \left( |\rho_1^{(o)}\rangle\rangle, \dots, |\rho_N^{(o)}\rangle\rangle \right). \end{aligned} \quad (7)$$

This reconstruction formula is valid only if the matrix  $\mathbb{M}^{(i)}$  is invertible, thereby imposing a fundamental condition on the set of initial states. To guarantee informational completeness of the tomography, the number of prepared states  $N$  must satisfy  $N \geq d^2$ , as the vectors are elements of a  $d^2$ -dimensional Bloch-Fano space. When  $N$  exceeds  $d^2$ , a symmetrization procedure can be applied [42], yielding the modified relation

$$\underline{\mathbb{M}}^{(o)} = \hat{P}(t)\underline{\mathbb{M}}^{(i)}, \quad (8)$$

where the symmetrized input and output matrices are defined by

$$\underline{\mathbb{M}}^{(i,o)} = \mathbb{M}^{(i,o)}(\mathbb{M}^{(i)})^\dagger. \quad (9)$$

Combining Eqs. (8) and (9) allows us to reconstruct the evolution superoperator  $\hat{P}(t)$ ,

$$\hat{P}(t) = \underline{\mathbb{M}}^{(o)} \left( \underline{\mathbb{M}}^{(i)} \right)^{-1}. \quad (10)$$

It is important to emphasize that the process matrix  $\hat{P}(t)$ , is an intrinsic property of the system's dynamics. It uniquely defines the linear map that governs the evolution, irrespective of whether the input probe states are pure or mixed. Consequently, Eq. (8) remains valid for any set of input states that is “informationally complete”, i.e., a state set that spans the entire  $d^2$ -dimensional operator space. When this condition of informational completeness is met, Eq. (10) provides an exact determination of the evolution of an arbitrary quantum state.

## B. Experimental setup and protocol

The schematic of the experimental setup is shown in Fig. 1. The core of our system is a paraffin-coated spherical vapor cell, 3.7 cm in diameter, containing an isotopically enriched sample of  $^{87}\text{Rb}$ . The cell is heated to 38 °C, corresponding to an atomic density of approximately  $9 \times 10^9$  atoms/cm<sup>3</sup> [43], and is placed inside a magnetic shield consisting of three cylindrical layers of mu-metal and a single cubic layer of ferrite, providing a shielding factor on the order of  $10^6$  [43]. Inside the shield, three orthogonal pairs of magnetic-field coils are

mounted (not shown). The coils allow for compensation of residual fields and the generation of pulses of non-oscillating magnetic fields along the  $x$ -,  $y$ -, and  $z$ -axes. An additional pair of Helmholtz coils produces an oscillating magnetic field with amplitude exceeding 25 G along the  $y$ -axis. This field induces a quadratic Zeeman effect without notable linear contributions (see Ref. [43] for details).

Illumination of the rubidium atoms is provided by three lasers. The first, a distributed-feedback (DFB) diode laser, serves as the probe for measuring atomic states. The second, a Fabry-Pérot extended-cavity diode laser (ECDL), serves as the pump laser to prepare specific input states. The third, a Ti:Sapphire laser, operates as the repump laser to prevent population trapping in dark hyperfine states. The wavelengths of all three lasers are independently controlled and stabilized; the pump and probe lasers use a dichroic atomic vapor laser lock [44], while the repump laser is frequency-locked via an internal module. Wavelength monitoring is carried out using a wavemeter for all lasers, supplemented by saturated absorption spectroscopy for the pump and probe lasers.

Laser beam intensities are passively controlled with high-quality crystal polarizers and half-wave plates, and dynamically modulated using three acousto-optic modulators. The lasers are temporarily switched off during the application of magnetic-field pulses. To generate a specific quantum state in the vapor, the pump light propagates along the  $x$ -axis and is circularly polarized using a Glan-Thompson linear polarizer followed by a quarter-wave plate. The repump light also propagates along the  $x$ -axis and is linearly polarized along the  $z$ -axis during the interaction with atoms. The probe light traverses the atoms along the  $z$ -axis and is linearly polarized along the  $y$ -axis by a Glan-Thomson linear polarizer placed before the shield. The probe-light polarization rotation after passing through the medium is measured with a balanced polarimeter consisting of a Wollaston prism and a balanced photodetector.

Reconstruction of the process superoperator  $\hat{P}(t)$  via Eq. (8) requires knowledge of both the  $N$  input states and their corresponding outputs, i.e., a total of  $2N$  quantum state tomography (QST) measurements. For the qutrit system investigated here ( $d = 3$ ), realized in the  $f = 1$  ground-state manifold of  $^{87}\text{Rb}$ , we choose an informationally complete set of  $N = 15$  input states that guarantees the invertibility of the matrix  $\mathbb{M}^{(i)}$ . The set consists of the three computational-basis states together with twelve equal-weight superpositions

$$|\psi_k\rangle = \left\{ \begin{aligned} &|i\rangle, \\ &\frac{1}{\sqrt{2}}(|i\rangle + e^{i\phi}|j\rangle), \end{aligned} \right. \quad (11)$$

where  $i, j \in \{-1, 0, 1\}$  index the qutrit levels, and  $\phi \in \{0, \pi/2, \pi, 3\pi/2\}$  ensures phase diversity. Because these 15 states span the full nine-dimensional Bloch space of a qutrit, they render the tomography protocol both complete and numerically stable, ensuring an unambiguous reconstruction of  $\hat{P}(t)$  with the desired precision.

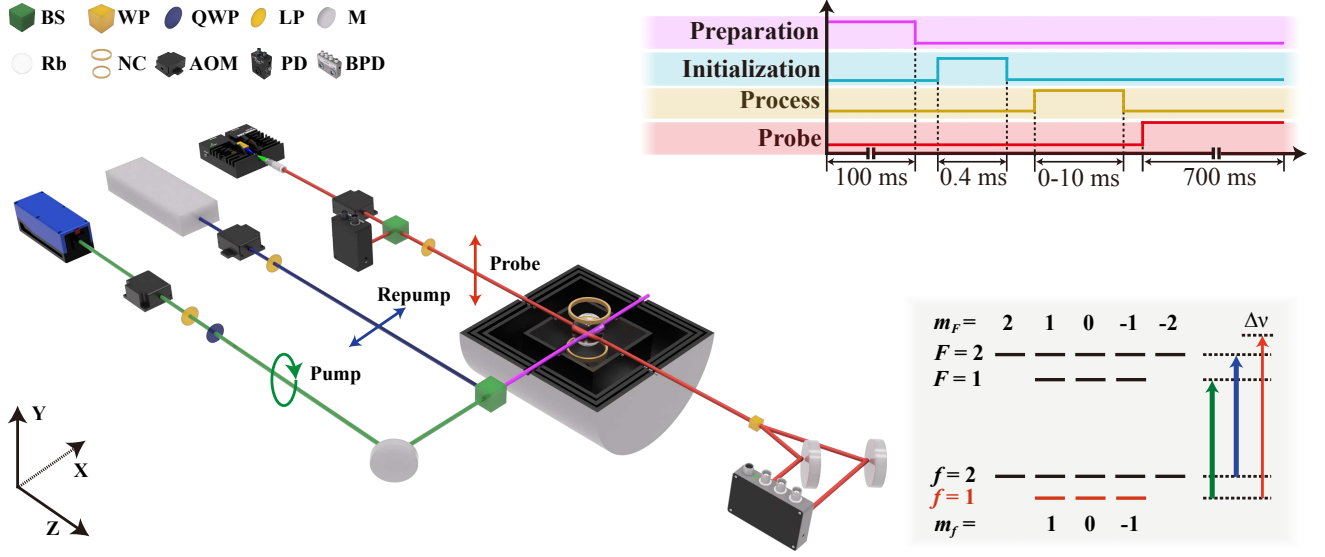


FIG. 1. Simplified scheme of the experimental setup used for the quantum-process tomography (Liouvillian reconstruction); the experimental sequence used for the reconstruction; and an energy-level diagram for the  $^{87}\text{Rb}$  D1 line, with measured qutrit marked in red, along with the pump- (green arrow), probe- (red arrow), and repump-light (blue arrows) tunings. During the first (preparation) stage (purple trace), the atoms are spin-polarized along the  $x$ -axis using the pump and repump light. In the next (initialization) stage (blue trace), one of fifteen input states is prepared. In the third (process) stage (yellow trace), a quantum process to be measured is applied to these special initial states. In the fourth (probe) stage, the probe light and the longitudinal magnetic field are turned on, and the polarization-rotation signal is recorded. While using the QST technique [42], a single quantum state can be completely reconstructed, performing the operation for the whole set of input and output states enables determination of the the corresponding quantum process. BS stands for a beam splitter; WP is a Wollaston prism; QWP is a quarter-wave plate; LP is a Glan-Thomson linear polarizer; M denotes a mirror; Rb is a paraffin-coated vapor cell filled with  $^{87}\text{Rb}$ ; NC stands for coils inducing nonlinear Zeeman effect; AOM is an acousto-optic modulator; PD is a photodiode; and BPD is a balanced photodetector.

The QPT sequence starts with spin polarization. A 100 ms optical-pumping pulse drives the atomic population into a well-defined spin state oriented along the  $x$ -axis (pumping within the  $f = 1$  ground-state hyperfine level), while simultaneous repump illumination prevents atoms from accumulating in the dark  $f = 2$  level. The polarized ensemble is then rotated into each of the 15 target input states defined in Eq. (11) by applying suitable combinations of a strong oscillating and a weak static magnetic field. Each prepared state is characterized by QST following the procedure of Ref. [42] (see the Supplementary Information (SI) [45] for state-preparation fidelities). Once the input states are certified, they are subjected to the process under study, and the corresponding output states are measured with the same QST protocol. With  $N = 15$  inputs, the full QPT therefore entails  $2N = 30$  QST runs, and every state reconstruction relies on nine Faraday-rotation traces (each trace may be an average of many measurements).

### III. LIOUVILLIAN RECONSTRUCTION

In our experiment, the main goal is to characterize the contributions to the system's evolution arising both from the controlled unitary dynamics and from uncontrolled

relaxation effects. Thus, our first objective is to separate the controlled unitary evolution generated by the magnetic fields we apply from the uncontrolled residual effects and intrinsic dissipation present in the system.

To formalize this, we present the Liouvillian superoperator as

$$\hat{\mathcal{L}}(t) = -i \left( \hat{H}_C(t) + \hat{H}_R \right) - \hat{R} = -i\hat{H}_C(t) - \hat{R}_T, \quad (12)$$

where  $\hat{H}_C(t)$  is the controlled (time-dependent) Hamiltonian driving the desired unitary evolution,  $\hat{H}_R$  is a time-independent Hamiltonian superoperator corresponding to residual uncontrolled fields, and  $\hat{R}$  describes the intrinsic dissipative relaxation channels (the time independence of the two latter superoperators is an assumption of our model). In turn, the effective total relaxation superoperator  $\hat{R}_T = i\hat{H}_R + \hat{R}$  combines both the intrinsic dissipation and relaxation associated with (principally) unitary yet uncontrollable evolution into a single term. In general, the unitary evolution can be mitigated by implementing such techniques as spin echo [46, 47]. Here, however, we incorporate it into the operator  $\hat{R}_T$ .

The decomposition provides a practical framework for analyzing system dynamics by comparing evolutions with and without the controlled Hamiltonian [13, 30]. Although straightforward in the superoperator formalism,

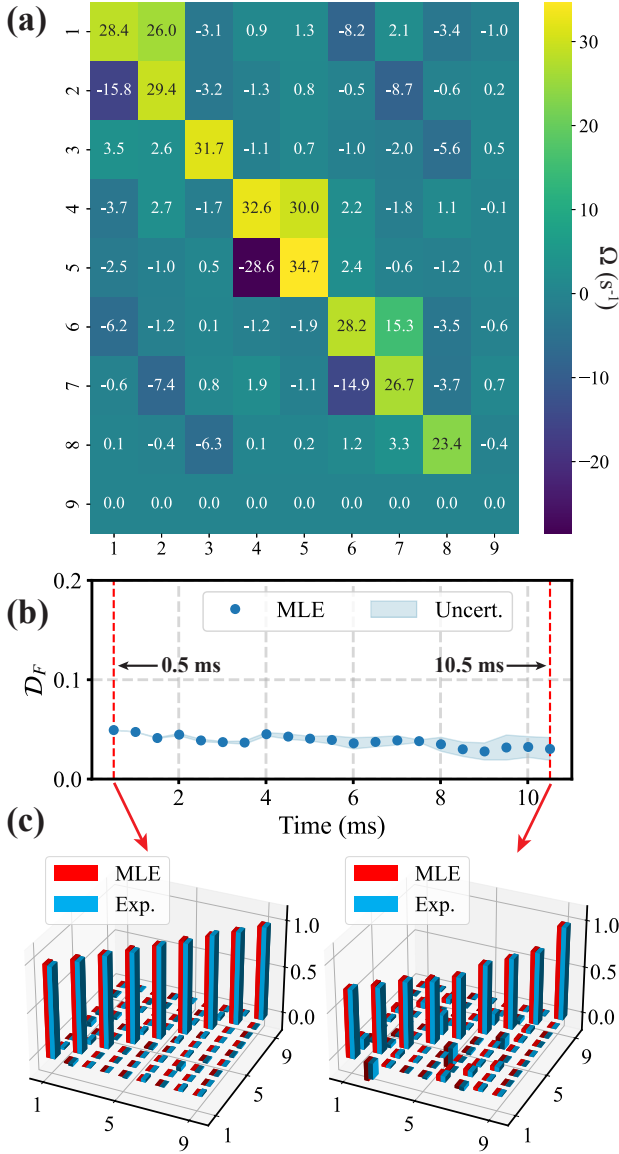


FIG. 2. (a) Reconstruction of the effective total relaxation superoperator  $\hat{R}_T$  via the MLE protocol. (b) The relative error  $\mathcal{D}_F$  with the uncertainty (Uncert.) quantifies the difference between the process matrix  $\hat{P}(t)$  obtained from experimental measurements and the simulation results via MLE over time. (c) The bar charts visually compare the experimental process matrix  $\hat{P}_{Exp.}$  (blue bar) and simulation via MLE  $\hat{P}_{MLE}$  (red bar) at  $t = 0.5, 10.5$  ms, and illustrate their deviations respectively.

interpreting this decomposition directly on the density-operator level is more involved (details and formal derivations are provided in Appendix B.)

In a simplified scenario where the Liouvillian is time-independent, a measurement at a single evolution time  $t'$

can be directly used to reconstruct the process matrix as

$$\hat{\mathcal{L}} = \frac{1}{t'} \log(\hat{P}(t')) = \frac{1}{t'} \log \left[ \underline{\mathbb{M}}^{(o)} \left( \underline{\mathbb{M}}^{(i)} \right)^{-1} \right], \quad (13)$$

where the second equality uses the symmetrized state matrices [see Eq. (8)]. This approach provides a straightforward estimate of the Liouvillian.

When measurements at multiple evolution times are available, it is advantageous to employ maximum-likelihood estimation (MLE) [18, 48–50], which refines the Liouvillian by minimizing the discrepancy between the experimentally determined and theoretically predicted processes over the entire data set. For a time-independent Liouvillian, and using Eq. (12), the cost function minimized in the MLE procedure can be defined as [48]

$$\begin{aligned} \Delta^2(\hat{\mathcal{L}}) &= \sum_n \left\| \exp(\hat{\mathcal{L}} t_n) - \hat{P}(t_n) \right\|_F^2 \\ &= \sum_n \left\| \exp \left[ - \left( i\hat{H}_C + \hat{R}_T \right) t_n \right] - \hat{P}(t_n) \right\|_F^2, \end{aligned} \quad (14)$$

where  $\|\cdot\|_F$  denotes the Frobenius norm and  $\hat{P}(t_n)$  are the process matrices reconstructed from the experiment at times  $t_n$ . This cost function measures the cumulative deviation between the predicted and measured processes.

To assess the quality of Liouvillian reconstruction and to compare process matrices, we employ the normalized Frobenius distance [48, 49] defined as

$$\mathcal{D}_F(\hat{A}, \hat{B}) = \frac{\left\| \hat{A} - \hat{B} \right\|_F}{\left\| \hat{B} \right\|_F}, \quad (15)$$

where  $\hat{A}$  and  $\hat{B}$  are superoperators corresponding to either measured and estimated process matrices or reconstructed and theoretical Liouvillian superoperators. In our work, we consider two main applications of this metric. First, when comparing evolution of process matrices,  $\hat{B}$  serves as the predicted process matrix generated by the reconstructed Liouvillian at different evolution times, acting as a reference for the measured process matrix  $\hat{A}$ . Second, when comparing Liouvillian superoperators, the reconstructed operator  $\hat{A}$  is compared to a reference theoretical Liouvillian  $\hat{B}$  reflecting known physical conditions. Because the Frobenius norm  $\left\| \hat{A} - \hat{B} \right\|_F$  measures absolute error, the normalized distance  $\mathcal{D}_F$  naturally quantifies relative error.

#### A. Estimation of the dissipator $\hat{R}_T$

As established in the proceeding section, the effective total relaxation superoperator  $\hat{R}_T$  is assumed to be time-independent and unaffected by any controllable interac-

tions. Accordingly, we first reconstruct  $\hat{R}_T$  in a dedicated set of measurements with all external control fields turned off, ensuring that no additional perturbations influence the process. Once  $\hat{R}_T$  has been characterized, it is used in subsequent experiments to isolate and determine the controlled Hamiltonian superoperator  $\hat{H}_C(t)$ , as detailed in Eq. (12).

From the experimental perspective, each state is measured at least three times to ensure statistical reliability. The intensity of the probe beam is fixed at  $10 \mu\text{W}/\text{cm}^2$ , with a frequency blue-detuned by 50 MHz from the atomic transition to minimize the probe-induced perturbation of the atomic state. Moreover, QPT is inherently susceptible to errors arising from imperfect state preparation and measurement (SPAM). A common method to mitigate SPAM errors is self-consistent QPT [18, 51, 52]. Here, however, our approach involves full reconstruction of both input and output quantum states for each experimental instance, complemented by pre-calibrated measurement settings, thereby mitigating SPAM-induced systematic errors.

Figure 2(a) shows the reconstructed relaxation superoperator  $\hat{R}_T$ , determined in the absence of all controllable external fields to isolate the system's intrinsic dynamics. This reconstruction is based on process matrices measured from 0.5 to 10.5 ms evenly spaced by 0.5 ms. The final, time-independent Liouvillian is obtained via the MLE procedure that minimizes the cost function in Eq. (14), in the absence of the controlled Hamiltonian ( $\hat{H}_C = 0$ ).

Because the total population of the atomic ensemble is conserved, the trace of the density matrix must remain unity throughout the evolution. Consequently, this trace preservation condition imposes a strict constraint on the structure of the relaxation superoperator, such that the elements in its ninth row representing population leakage must vanish identically. This is confirmed by the experimentally reconstructed relaxation superoperator in Fig. 2(a).

The remaining elements of  $\hat{R}_T$  encode the couplings and decay rates of the eight independent components of the state vector (see Appendix C). In most experiments involving room-temperature atoms in paraffin-coated cells, after compensating for residual magnetic fields and magnetic-field gradients, it is common to assume a uniform relaxation model. This relaxation can typically be estimated from the decay of the magnetization (see SI). Under such assumptions, the relaxation appears as a diagonal relaxation superoperator. As shown in Fig. 2(a), this is a good first-order approximation. Based on the experimental results, the isotropic part of the relaxation is approximately  $29.4_{-2.3}^{+2.3} \text{s}^{-1}$ . However, in addition to the diagonal elements of  $\hat{R}_T$  indicating the uniform relaxation, there are several significant off-diagonal elements of the superoperator. Motivated by the elements, we performed a more detailed analysis of

the relaxation in our system.

Generally,  $\hat{R}_T$  comprises three contributions: (i) residual magnetic fields inducing Larmor precession, (ii) isotropic relaxation at rate  $\gamma_i$ , and (iii) decoherence due to magnetic-field inhomogeneities, characterized by rates  $\gamma_k$  for  $k = x, y, z$ .

To model decoherence, we generalize the qubit dephasing channel by introducing three independent Lindblad operators  $\hat{L}_k = \sqrt{\gamma_k} \hat{F}_k$ , where  $\hat{F}_k$  are angular momentum operators along each axis. This model provides a richer description compared to the uniform relaxation approach.

From Fig. 2(a), we estimate residual Larmor frequencies  $\Omega_L/2\pi = \{-0.397_{-0.011}^{+0.011}, 0.3071_{-0.0091}^{+0.0091}, 2.511_{-0.034}^{+0.034}\} \text{Hz}$ , dephasing rates  $\gamma_k = \{7.0_{-1.0}^{+1.0}, 7.9_{-1.1}^{+1.1}, 6.6_{-1.3}^{+1.3}\} \text{s}^{-1}$ , and isotropic relaxation rate  $\gamma_i = 13.3_{-1.6}^{+1.6} \text{s}^{-1}$ . These rates were extracted from 1000 simulated measurements, providing meaningful error estimates. The theoretical relaxation superoperator reconstructed from these parameters (see Fig. 3 in SI) shows good agreement with that reconstructed from the MLE of the experimental data, highlighting the limitations of a purely isotropic relaxation model.

Having fully characterized the relaxation superoperator  $\hat{R}_T$  from its individual matrix elements, we next validate its overall physical consistency. To do so, we use the reconstructed  $\hat{R}_T$  to simulate the time evolution of the process matrix, yielding a predicted process  $\hat{P}_{\text{MLE}}(t) = \exp(-\hat{R}_T t)$ . This simulated process is then compared with experimentally measured process matrices.

Figure 2(b) shows the relative error  $\mathcal{D}_F$  between the simulated and measured process matrices across the entire evolution time (blue points). The results demonstrate a small quantitative disagreement, with a maximum relative error bounded at  $0.04929_{-0.00016}^{+0.00016}$ . For a more intuitive comparison, the bar charts in Fig. 2(c) provide a visual snapshot of the process matrix  $\hat{P}(t)$  caused by the relaxation at two representative times,  $t = 0.5 \text{ms}$  and  $t = 10.5 \text{ms}$ . The strong agreement between the simulated dynamics derived from our MLE analysis (red bars) and the experimental measurements (blue bars) confirms that the reconstructed superoperator  $\hat{R}_T$  provides an accurate and physically consistent model of the total relaxation process.

## B. Time-independent Hamiltonian

Knowledge of the time-independent relaxation term  $\hat{R}_T$  enables the estimation of the control Hamiltonian. In the basic scenario considered in this section, we assume that the superoperator  $\hat{H}_C$  is time independent.

As a test platform for this analysis, we consider a Hamiltonian governed purely by the quadratic Zeeman

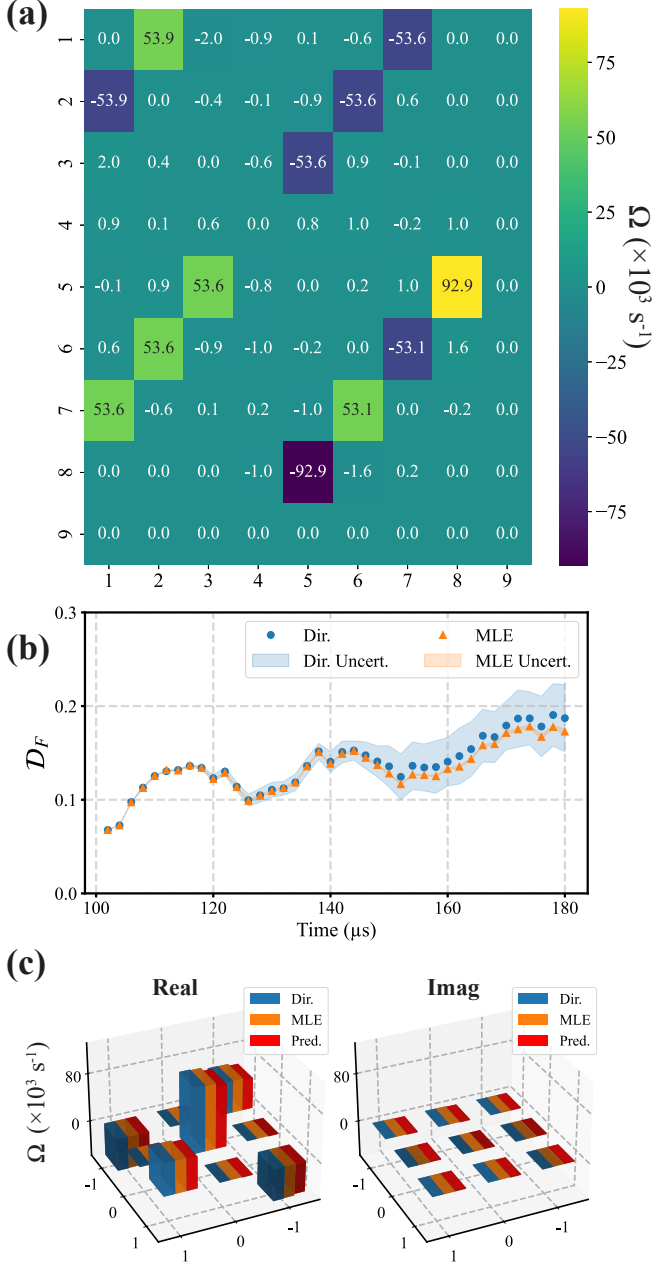


FIG. 3. (a) The Hamiltonian superoperator reconstruction using the MLE approach. (b) Normalized Frobenius distance between the experimentally measured process superoperators and those generated from the estimated  $\hat{H}_C$  using direct reconstruction (blue dots) and MLE (orange triangles). The blue (Dir. Uncert.) and orange (MLE Uncert.) shaded regions represent the associated uncertainties, respectively. (c) Comparison of the real and imaginary parts of Hamiltonian operators. The red bars show the predicted Hamiltonian (Pred.) based on the known setup parameters of the coil geometry and system response [43], while the orange (MLE) and blue (direct reconstruction) ones represent the Hamiltonians extracted from the estimated superoperators. The relative error, quantified by the normalized Frobenius distance between the predicted and MLE-based Hamiltonian, is  $\mathcal{D}_F^{\text{MLE}} = 0.05657^{+0.00087}_{-0.00087}$ , while for direct reconstruction it is  $\mathcal{D}_F^{\text{Dir}} = 0.068^{+0.015}_{-0.015}$ .

effect. This is realized experimentally by applying a pulse of a rapidly oscillating, sufficiently strong magnetic field, which introduces both linear and quadratic Zeeman effects. In the technique described in Ref. [43], rapid oscillation causes the linear Zeeman contribution to average out over each period due to the field's alternating sign, while the quadratic component accumulates coherently. In turn, the linear term can be effectively canceled by shaping the pulse envelope appropriately. Importantly, the oscillation frequency is several orders of magnitude higher than the characteristic time scales of the ground-state dynamics. This allows the pulse to be treated as a quasi-static, isolated quadratic Zeeman perturbation from the perspective of the slow atomic evolution, which can be described by an effective, time-independent Hamiltonian  $\hat{H}_C$ .

To reconstruct the controlled Hamiltonian superoperator  $\hat{H}_C$ , we prepare the same set of initial states as used in the reconstruction of the total relaxation superoperator  $\hat{R}_T$ . These states evolve over a variable time  $t$  under the action of the effective Hamiltonian  $\hat{H}_C$ . The output states are then measured. Measurements are performed for various pulse durations, ranging from 100 to 180  $\mu\text{s}$ . This range balances the limitations of the pulse generator (restricting shorter pulses) against increasing atomic relaxation effects at longer times.

The controlled Hamiltonian superoperator  $\hat{H}_C$  is reconstructed using two complementary methods. In the direct linear inversion approach, we determine  $\hat{H}_C$  from the measured input-output data at each evolution time and then average the individual estimates. This procedure is quick and requires no numerical optimization, but because it does not impose any physical constraints, experimental noise can produce a non-Hermitian, and therefore non-physical, operator. To address this problem, we apply a least-squares fitting procedure with a Hermiticity constraint to obtain a physically consistent estimate. In practice, we begin with a general Hermitian operator, where each matrix element is determined via a linear inversion mapping from the corresponding superoperator to the operator space (See Appendix C for details). The second method is that we employ a constrained MLE procedure to ensure a physically valid result in the beginning. Here we fit the entire data set minimizing the cost function (14) while fixing the previously determined relaxation superoperator  $\hat{R}_T$  and explicitly restricting the search to Hermitian operators. As the optimization is carried out within the standard MLE framework, the final estimate  $\hat{H}_C^{\text{MLE}}$  is guaranteed to be Hermitian by construction.

Since the elements of the Hamiltonian superoperator  $\hat{H}_C$  are only filled with imaginary numbers, Figure 3(a) shows the imaginary part of  $\hat{H}_C$  reconstructed by MLE using the process matrices for all coherent-evolution times between 100 and 180  $\mu\text{s}$ . Again, the trace-preserving condition enforces zero entries in the

ninth row of the superoperator matrix, and the diagonal elements vanish identically to ensure strict unitarity of the Hamiltonian-induced evolution. Crucially, the off-diagonal elements quantitatively encode the coupling strengths between state vector components mediated by the specific Hamiltonian interaction. Under the isolated quadratic Zeeman perturbation, Figure 3(a) reveals that the magnitude and spatial distribution of these off-diagonal elements eventually converge to the theoretical structure of the superoperator derived for this perturbation [see Eq. (C.4) in Appendix. C].

To assess the physical consistency of the reconstructed dynamics, we simulate the time evolution of the process matrix using the previously determined relaxation superoperator  $\hat{R}_T$  and the controlled Hamiltonian  $\hat{H}_C$  estimated via both the direct reconstruction and MLE. The evolution is governed by  $\hat{P}_{\text{Dir/MLE}}(t) = \exp\left\{-(i\hat{H}_C^{\text{Dir/MLE}} + \hat{R}_T)t\right\}$ . We then evaluate the relative errors between the simulated and experimentally measured process matrices. As illustrated in Fig. 3(b), the relative errors for the direct reconstruction and MLE are bounded by  $0.190^{+0.034}_{-0.034}$  and  $0.1781^{+0.0018}_{-0.0018}$ , respectively. Both methods agree well with experimental data, with MLE providing marginally improved accuracy.

Finally, we compared the two approaches with the theoretical predictions based on coil geometry and system response. As shown in Fig. 3(c), the reconstructed Hamiltonian operator corresponding to  $\hat{H}_C$  from both approaches aligns closely with theoretical predictions. The MLE method yields a slightly smaller relative error  $\mathcal{D}_F^{\text{MLE}} = 0.05657^{+0.00087}_{-0.00087}$  than the direct reconstruction approach  $\mathcal{D}_F^{\text{Dir}} = 0.068^{+0.015}_{-0.015}$ . As observed, a tiny relative error persists between the prediction and the two reconstructed Hamiltonians even after eliminating  $\hat{R}_T$ . We think that although we initially assumed that the system's relaxation was unaffected by any external interaction, the magnetic field applied to create the nonlinear Zeeman effect introduces additional decoherence channels simultaneously, due to spatial inhomogeneities in the field's magnitude and orientation. These extra decoherence contributions, which originate from the relaxation superoperator, were erroneously attributed to the Hamiltonian superoperator. In our experimental framework, the MLE inherently searches for the physically most consistent Hamiltonian superoperator (including spurious decoherence contributions) to minimize the relative error of the process matrices throughout the evolution. The direct reconstruction method averages all possible superoperators (both physically consistent and inconsistent) before selecting the most physically plausible result. Nevertheless, both methodologies demonstrate strong robustness in the reconstruction of time-independent Hamiltonians, despite their differing sensitivities to decoherence effects.

### C. Time-dependent Hamiltonian

We now relax the initial assumption that the Hamiltonian is time independent and reconstruct the controlled Hamiltonian superoperator  $\hat{H}_C$  in the presence of time-varying external fields. To accomplish this, the theoretical model presented in Sec. II A must be adapted.

Because a continuous measurement of a quantum system is fundamentally impossible, we adopt a coarse-grained approach to the system's temporal evolution by dividing it into small time intervals  $\Delta t$ . Within each interval, the interaction is assumed to be constant. This discretization requires prior knowledge of the characteristic dynamical timescales of the quantum process under investigation. For example, in the presence of an oscillating magnetic field, the time step  $\Delta t$  must be short enough to capture oscillations adequately, i.e., too large  $\Delta t$  could fail to resolve important dynamics. This approach allows us to choose a time grid that balances capturing essential dynamics with practical measurement density.

Taking into account the discretization, Eq. (3) can be reformulated as

$$\begin{aligned} |\rho(t_n)\rangle\rangle &= \mathcal{T} \left\{ \prod_{k=0}^{n-1} \exp(\hat{\mathcal{L}}_k \Delta t) \right\} |\rho(0)\rangle\rangle \\ &= \mathcal{T} \left\{ \prod_{k=0}^{n-1} \hat{P}_k \right\} |\rho(0)\rangle\rangle, \end{aligned} \quad (16)$$

where  $\hat{P}_k$  is the process superoperator describing evolution from time  $t_k$  to  $t_{k+1}$ . Measuring the state matrices at these discrete times and applying Eq. (6), we find

$$\mathbb{M}^{(n+1)} = \hat{P}(t_n; t_{n+1}) \mathbb{M}^{(n)} = \hat{P}_n \mathbb{M}^{(n)}. \quad (17)$$

Using both direct and MLE reconstruction methods, the time-dependent controlled Hamiltonian superoperator  $\hat{H}_C(t_n)$  can be extracted from the experimentally determined  $\hat{P}_n$  at each time step.

Figure 4(a) evaluates the accuracy of our time-dependent reconstruction by plotting the relative error,  $\mathcal{D}_F$ , between the experimentally measured process superoperators and those simulated using the reconstructed Hamiltonian,  $\hat{H}_C(t)$ . The relative error of the process matrix reaches its maximum value for the case of direct reconstruction with  $\mathcal{D}_F = 0.146^{+0.032}_{-0.032}$  and MLE with  $\mathcal{D}_F = 0.146^{+0.011}_{-0.011}$  at  $t = 64 \mu\text{s}$ . To investigate the source of this discrepancy, we compare the reconstructed Hamiltonian at this specific time point against the predicted reference Hamiltonian, as shown in Fig. 4(b). The predicted one is determined from preset current magnitudes, using the known relationship between current and magnetic strength in three orthogonal directions. The relative errors in the Hamiltonian reconstruction itself are found to be  $\mathcal{D}_F^{\text{MLE}} = 0.215^{+0.042}_{-0.042}$  for the MLE method and  $\mathcal{D}_F^{\text{Dir}} = 0.212^{+0.022}_{-0.022}$  for the direct method. The close agreement between the error in the overall process and

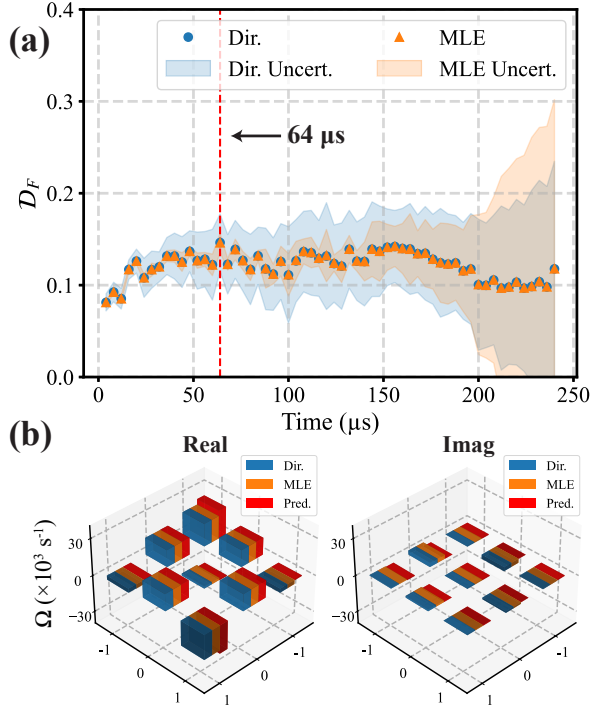


FIG. 4. (a) Relative error between the experimentally measured process superoperators and those generated from the estimated time-dependent Hamiltonian  $\hat{H}_C(t)$  using direct reconstruction (blue dots) and MLE (orange triangles); and the corresponding uncertainties represented by the blue (Dir. Uncert.) and orange (MLE Uncert.) shaded regions. (b) Comparison of the real and imaginary parts of Hamiltonian operators at  $t = 64 \mu\text{s}$ . The blue, orange, and red bars represent the Hamiltonian operator via direct reconstruction, MLE, and prediction, respectively. The predicted Hamiltonian is derived from known current-to-magnetic strength ratios in three directions, computed using current magnitudes at preset time points. The corresponding relative error between the predicted and MLE-based Hamiltonian superoperators is  $\mathcal{D}_F^{\text{MLE}} = 0.215^{+0.042}_{-0.042}$ , while for direct reconstruction it is  $\mathcal{D}_F^{\text{Dir}} = 0.212^{+0.022}_{-0.022}$ .

the error in the Hamiltonian reconstruction based on a single point suggests that the deviation observed in the process evolution is primarily driven by inaccuracies in the Hamiltonian determination. These underlying reconstruction errors likely originate from a combination of systematic uncertainties, such as experimental noise and approximations in the superoperator mapping.

#### D. Multiparameter estimation

The general time-dependent Hamiltonian reconstruction technique can be readily adapted for metrological applications, particularly enabling the simultaneous estimation of multiple parameters.

In this context, we assume the functional form of the control Hamiltonian is known, while certain parameters

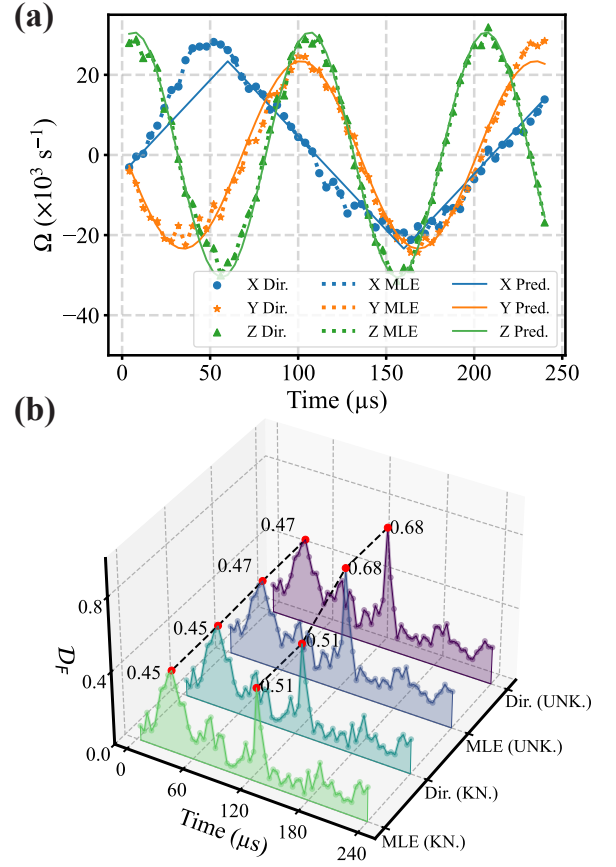


FIG. 5. (a) Example of multiparameter estimation using time-dependent Hamiltonian reconstruction. Magnetic fields are applied in all three orthogonal directions with distinct waveforms, amplitudes, phases, and frequencies. Solid lines serve as references, representing the expected Larmor frequencies based on the known applied magnetic fields. Dotted lines and points indicate parameter estimates obtained via MLE and direct reconstruction, respectively. (b) Relative errors between the predicted and reconstructed superoperators using both the direct reconstruction and MLE, under conditions with known (KN.) and unknown (UNK.) Hamiltonian form constraints [Eq. (18)]. The purple and blue lines denote the relative errors obtained with unknown Hamiltonian constraints, while the cyan and green lines represent the errors computed with known Hamiltonian constraints. All four scenarios are annotated with relative errors at  $t = 36 \mu\text{s}$  and  $t = 124 \mu\text{s}$  (red points).

remain unknown and need to be estimated. Specifically, we consider a model Hamiltonian of the form

$$\hat{H}_C(t) = \sum_k \Omega_k(t) \hat{F}_k, \quad (18)$$

where  $\hat{F}_k$  denotes the angular momentum operator along the  $k$ -axis, and  $\Omega_k(t)$  is the time-dependent Larmor frequency treated as a free parameter.

To estimate these parameters, we apply both the previously described methods. In the direct reconstruction approach, the time-dependent Hamiltonian reconstruc-

tion algorithm is followed by a least-squares fitting procedure to find the optimal set of model parameters  $\Omega_k(t)$  that best match the experimental data. In the MLE approach, we use the cost function defined in Eq. (14), with the additional constraint that the Hamiltonian takes the parametric form of Eq. (18).

To demonstrate the power and precision of our technique in a complex, multiparameter scenario, we simultaneously applied three distinct, time-varying magnetic fields along the orthogonal  $x$ -,  $y$ -, and  $z$ -axes. This test was designed to be particularly challenging, incorporating a mix of frequencies (5, 7.5, and 10 kHz), initial phases (0,  $\pi$ , and  $\pi/2$ ), and waveforms (a triangular wave along the  $x$ -axis and sinusoidal waves along the  $y$ - and  $z$ -axes).

Figure 5(a) presents the results, comparing the preset applied Larmor frequencies (solid lines) against the parameters extracted from the experimental data. The parameters obtained through both MLE (dotted lines) and direct reconstruction (points) show excellent agreement with the reference fields, accurately tracking the unique evolution of each component. A minor deviation is observable for the  $x$ -axis during the initial 64  $\mu$ s. This transient behavior is attributed to the finite response time of the current supply. After this brief stabilization period, the reconstructed parameters converge to the expected values, confirming the method's capability to faithfully reconstruct multiple, overlapping time-dependent signals.

Finally, we systematically examine the impact of the known/unknown control Hamiltonian form constraint on the accuracy of superoperator reconstruction. As illustrated in Fig. 5(b), the relative errors for the Hamiltonian superoperator exhibit a systematic reduction when the reconstruction is constrained by the known Hamiltonian form (cyan and green lines) compared to the unknown situations (purple and blue lines), across both direct reconstruction and MLE. This shows that enforcing physical constraints derived from the underlying Hamiltonian structure significantly enhances reconstruction fidelity. Furthermore, note that the maxima of the relative error of Hamiltonian reconstruction in the above four situations emerge concurrently at the two specific evolution times. The first maxima occur at  $t = 36 \mu$ s, predominantly attributable to transient instabilities in the initial current supply, which induce perturbations in the early dynamics of the system. The second manifests at  $t = 124 \mu$ s, resulting from the decrease in the applied total Larmor frequency. This reduction exacerbates the relative error due to normalization artifacts, as the error metric scales inversely to the magnitude of the reference [see Eq. (15)].

#### IV. CONCLUSION

We have introduced and experimentally demonstrated a quantum-process-tomography protocol that overcomes

key limitations of conventional methods. By casting the Lindblad master equation in the Bloch-Fano representation, we developed a computationally efficient scheme that enables full reconstruction of time-dependent Liouvillian superoperators while greatly reducing measurement and analysis overheads. Tests on a  $^{87}\text{Rb}$  qutrit confirmed the accuracy and versatility of the method. Because the procedure is representation-independent, it can be extended to higher-dimensional qudits without conceptual changes.

The QPT method implemented here can be used to directly reveal Liouvillian exceptional points [53], as theoretically predicted in [54] for room-temperature alkali-metal vapors modeled as a qutrit or quartit, analogous to the application of QPT for identifying such points in few-qubit quantum circuits [47].

Beyond these immediate achievements, our work paves the way for several future directions. An outstanding challenge in quantum science is the characterization of non-Markovian dynamics, where memory effects in the environment play a significant role and the standard Lindblad framework becomes inadequate [23, 55, 56]. Owing to its sub-millisecond time resolution, our scheme can be applied to successive short windows to reconstruct the process tensor, a mathematical construct that fully describes such memory effects, thereby providing direct experimental access to temporal correlations that characterize non-Markovian noise [23, 55].

A further application lies in the quantitative benchmarking of analogue quantum simulators and sensors. Many state-of-the-art platforms, such as Rydberg-atom arrays [57] or trapped ion [58], operate in regimes where coherent and dissipative processes compete. Reconstructing the Liouvillian under different operating conditions would allow experimentalists to validate microscopic models of their devices, identify unexpected loss channels, and refine parameter regimes for optimal performance. Because the reconstruction is measurement-efficient, such benchmarking could be repeated throughout extended experimental runs, providing a practical tool for long-term calibration and drift compensation.

Finally, the rich data produced by our method are well suited to machine-learning analysis. Deep-learning models have been used to accelerate state tomography [59], identify correlated noise [60], and design control pulses [61, 62]. Training these models on time-resolved Liouvillian estimates could reveal subtle correlations, predict instabilities before they affect performance, or suggest improved operating points. By combining efficient tomography with data-driven inference, the present approach provides a practical pathway toward the systematic characterisation, calibration, and optimisation of emerging quantum technologies.

## ACKNOWLEDGMENTS

The authors would like to thank Adam Miranowicz and Yintai Zhang for many stimulating discussions and valuable comments. This research was financially supported by the National Science Centre of Poland (NCN) within the Sonata Bis program (grant No. 2019/34/E/ST2/00440). M.K. would like to acknowledge support from the NCN under the Maestro Grant No. DEC-2019/34/A/ST2/00081.

## Appendix A: Bloch–Fano representation

For a  $d$ -level system the density operator  $\hat{\rho}$  can conveniently be expanded in the Bloch–Fano representation [39, 63]

$$\hat{\rho} = \frac{1}{d} \hat{\mathbb{1}}_d + \sum_{i=1}^{d^2-1} a_i \hat{\sigma}_i = \sum_{i=1}^{d^2} a_i \hat{\sigma}_i, \quad (\text{A.1})$$

where  $\hat{\mathbb{1}}_d$  is the  $d \times d$  identity and  $\{\hat{\sigma}_1, \dots, \hat{\sigma}_{d^2-1}\}$  are the generators of  $\text{SU}(d)$  (the generalized Pauli matrices). For compactness, we extend this set by defining  $\hat{\sigma}_{d^2} = \sqrt{2/d} \hat{\mathbb{1}}_d$ ; with the chosen normalization, all basis operators satisfy the orthogonality relation

$$\frac{1}{2} \text{Tr}(\hat{\sigma}_i \hat{\sigma}_j) = \delta_{ij}. \quad (\text{A.2})$$

The explicit matrices employed in this work are listed in the Supplementary Information.

Because the coefficients  $a_i = \frac{1}{2} \text{Tr}(\hat{\rho} \hat{\sigma}_i)$  form a real vector, it is natural to vectorize the density operators by writing  $|\rho\rangle\rangle \equiv (a_1, \dots, a_{d^2})^T$ . Equation (A.1) can then be read as an isomorphism between operators and vectors,

$$\hat{\rho} = \sum_{i=1}^{d^2} \rho_i \hat{\sigma}_i \iff |\rho\rangle\rangle_i = \rho_i, \quad (\text{A.3})$$

which we use throughout the superoperator formalism.

To complete the description, one needs to translate the Liouvillian into the superoperator formalism

$$\mathcal{L}(\hat{\rho}) \rightarrow \hat{\mathcal{L}} |\rho\rangle\rangle = -(\hat{H} + \hat{R}) |\rho\rangle\rangle, \quad (\text{A.4})$$

where the first term expands as follows:

$$\begin{aligned} [\hat{H}, \hat{\rho}] &= \sum_{i=1}^{d^2} [\hat{H}, \hat{\sigma}_i] \rho_i = \sum_{i,j=1}^{d^2} \frac{1}{2} \text{Tr}([\hat{H}, \hat{\sigma}_i] \hat{\sigma}_j) \rho_i \hat{\sigma}_j \\ &= \sum_{i,j=1}^{d^2} \hat{\sigma}_j \hat{H}_{ji} |\rho\rangle\rangle_i = \hat{H} |\rho\rangle\rangle, \end{aligned} \quad (\text{A.5})$$

with  $\hat{H}$  being a matrix with elements given by

$$\hat{H}_{ij} = \frac{1}{2} \text{Tr}([\hat{H}, \hat{\sigma}_j] \hat{\sigma}_i). \quad (\text{A.6})$$

Similarly second term in Eq. (A.4) is expanded as:

$$\begin{aligned} \sum_{\mu} \frac{1}{2} \{\hat{L}_{\mu}^{\dagger} \hat{L}_{\mu}, \hat{\rho}\} - \hat{L}_{\mu} \hat{\rho} \hat{L}_{\mu}^{\dagger} &= \\ &= \sum_{i,j=1}^{d^2} \frac{1}{2} \sum_{\mu} \text{Tr} \left( \left[ \frac{1}{2} \{\hat{L}_{\mu}^{\dagger} \hat{L}_{\mu}, \hat{\sigma}_i\} - \hat{L}_{\mu} \hat{\sigma}_i \hat{L}_{\mu} \right] \hat{\sigma}_j \right) \rho_i \hat{\sigma}_j \\ &= \sum_{i,j=1}^{d^2} \hat{\sigma}_j \hat{R}_{ji} |\rho\rangle\rangle_i = \hat{R} |\rho\rangle\rangle, \end{aligned} \quad (\text{A.7})$$

with

$$\hat{R}_{ij} = \frac{1}{2} \sum_{\mu} \text{Tr} \left( \left[ \frac{1}{2} \{\hat{L}_{\mu}^{\dagger} \hat{L}_{\mu}, \hat{\sigma}_j\} - \hat{L}_{\mu} \hat{\sigma}_j \hat{L}_{\mu} \right] \hat{\sigma}_i \right). \quad (\text{A.8})$$

With Eqs. (A.4)–(A.8) the Lindblad master equation is fully expressed in Bloch–Fano form, which is the starting point for the tomography protocol presented in the main text.

## Appendix B: Effective dissipation

Residual, slowly varying magnetic fields are unavoidable in most atomic-vapor experiments (e.g., due to imperfect or drifting shielding efficiency). Although these fields enter the dynamics through an additional Hamiltonian term, it is convenient to absorb their effect into an effective relaxation superoperator, defined by Eq. (12). In Liouville space this is merely a regrouping of terms, but translating the result back to operator language requires a new set of jump operators that reproduces the same evolution. The construction can be carried out within the Gorini–Kossakowski–Lindblad–Sudarshan (GKLS) formalism [30].

Working in the operator basis  $\{\hat{\sigma}_1, \dots, \hat{\sigma}_{d^2}\}$  introduced in Appendix A, a master equation may be written as

$$\begin{aligned} \frac{d\hat{\rho}}{dt} &= -i[\hat{H}_C(t), \hat{\rho}] - i[\hat{H}_R, \hat{\rho}] \\ &\quad - \sum_{i,j=1}^{d^2} \mathbb{C}_{ij} \left( [\hat{\sigma}_i, \hat{\rho} \hat{\sigma}_j^{\dagger}] + [\hat{\sigma}_i \hat{\rho}, \hat{\sigma}_j^{\dagger}] \right), \end{aligned} \quad (\text{B.1})$$

where  $\mathbb{C}_{ij}$  are the elements of the (generally complex) Kossakowski matrix  $\mathbb{C}$ . Unlike the standard presentation, the sum includes the basis element proportional to the identity,  $\hat{\sigma}_{d^2} = \sqrt{2/d} \hat{\mathbb{1}}_d$ , which is useful for the following construction.

Let us not rewrite the residual magnetic-field Hamiltonian  $\hat{H}_R$  using the generalized Pauli matrices,  $\hat{H}_R =$

$\frac{1}{2} \sum_k h_k \hat{\sigma}_k$  where  $h_k = \text{Tr}(\hat{H}_R \hat{\sigma}_k)$ . This allows us to present the second term in Eq. (B.1) as

$$\begin{aligned} -i[\hat{H}_R, \hat{\rho}] &= -\frac{i}{2} \sum_k h_k [\hat{\sigma}_k, \hat{\rho}] \\ &= -\frac{i}{2} \sum_k h_k ([\hat{\sigma}_k, \hat{\rho} \hat{\sigma}_{d^2}] + [\hat{\sigma}_k \hat{\rho}, \hat{\sigma}_{d^2}]). \end{aligned} \quad (\text{B.2})$$

Comparison between Eqs. (B.1) and (B.2) shows that the Hamiltonian contribution can be absorbed into the dissipator through the replacement

$$\mathbb{C}_{ij} \longrightarrow \mathbb{C}'_{ij} = \mathbb{C}_{ij} - \frac{i\sqrt{d}}{2\sqrt{2}} h_i (\delta_{j,d^2} - \delta_{i,d^2}). \quad (\text{B.3})$$

The transformation in Eq. (B.3) mixes the coherent and dissipative parts of the generator and may produce a Kossakowski matrix that is not positive semi-definite. This does not endanger complete positivity of the overall Liouvillian, as we have only redistributed terms without altering its action on  $\hat{\rho}$ . Diagonalising the modified matrix  $\mathbb{C}'$  yields an equivalent set of jump operators and rates in standard GKLS form, completing the translation from the effective superoperator  $\hat{R}_T$  back to ordinary operators.

### Appendix C: Hamiltonian reconstruction

The simplest way to estimate a quantum process is by direct reconstruction. Provided the Liouvillian is

time-independent over the interrogation time  $t$ , the evolution operator obeys Eq. (3) and one may write

$$\hat{\mathcal{L}} = \frac{1}{t} \log(\hat{P}(t)) = \frac{1}{t} \log(\underline{\mathbb{M}}^{(o)} (\underline{\mathbb{M}}^{(i)})^{-1}), \quad (\text{C.1})$$

where  $\underline{\mathbb{M}}^{(i)}$  and  $\underline{\mathbb{M}}^{(o)}$ , defined in Eq. (9), are the symmetrized matrices that contain, respectively, the input and the output states of the tomography protocol.

Before extracting the control Hamiltonian we subtract the effective relaxation superoperator, obtained as described in Sec. III A:

$$\hat{H}_C = i(\hat{\mathcal{L}} + \hat{R}_T). \quad (\text{C.2})$$

The resulting  $\hat{H}_C$  is an a priori unconstrained real matrix; experimental noise can therefore render it non-Hermitian. To enforce Hermiticity, we parametrize a general  $3 \times 3$  Hermitian operator

$$\hat{H} = \begin{pmatrix} H_1 & H_2 - iH_3 & H_4 - iH_5 \\ H_2 + iH_3 & H_6 & H_7 - iH_8 \\ H_4 + iH_5 & H_7 + iH_8 & H_9 \end{pmatrix}, \quad (\text{C.3})$$

with nine real parameters  $\{H_k\}_{k=1}^9$ .

Using Eq. (A.6) we convert  $\hat{H}$  to its superoperator representation. For the  $d = 3$  basis employed in this work one finds

$$\hat{H} = -i \begin{pmatrix} 0 & H_1 - H_6 & -2H_3 & H_8 & -H_7 & H_5 & -H_4 & 0 & 0 \\ H_6 - H_1 & 0 & 2H_2 & H_7 & H_8 & -H_4 & -H_5 & 0 & 0 \\ 2H_3 & -2H_2 & 0 & H_5 & -H_4 & -H_8 & H_7 & 0 & 0 \\ -H_8 & -H_7 & -H_5 & 0 & H_1 - H_9 & H_3 & H_2 & -\sqrt{3}H_5 & 0 \\ H_7 & -H_8 & H_4 & H_9 - H_1 & 0 & -H_2 & H_3 & \sqrt{3}H_4 & 0 \\ -H_5 & H_4 & H_8 & -H_3 & H_2 & 0 & H_6 - H_9 & -\sqrt{3}H_8 & 0 \\ H_4 & H_5 & -H_7 & -H_2 & -H_3 & H_9 - H_6 & 0 & \sqrt{3}H_7 & 0 \\ 0 & 0 & 0 & \sqrt{3}H_5 & -\sqrt{3}H_4 & \sqrt{3}H_8 & -\sqrt{3}H_7 & 0 & 0 \\ 0 & 0 & 0 & 0 & 0 & 0 & 0 & 0 & 0 \end{pmatrix}. \quad (\text{C.4})$$

Next, by equating the reconstructed superoperator with this form:

$$\hat{H}_{ij} = \left( \hat{H}_C(t) \right)_{ij}. \quad (\text{C.5})$$

Finally we equate the matrix elements of Eq. (C.4)

with those of the directly reconstructed  $\hat{H}_C$ , obtaining an overdetermined linear system for the parameters  $H_k$ . Solving this system in the least-squares sense yields the Hermitian Hamiltonian that is most consistent with the measured process.

[1] C. L. Degen, F. Reinhard, and P. Cappellaro, Quantum sensing, Rev. Mod. Phys. **89**, 035002 (2017).

[2] V. Giovannetti, S. Lloyd, and L. Maccone, Advances in

- quantum metrology, *Nat. Photonics* **5**, 222 (2011).
- [3] M. A. Nielsen and I. L. Chuang, *Quantum computation and quantum information* (Cambridge University Press, 2010).
  - [4] M. Lobino, D. Korystov, C. Kupchak, E. Figueroa, B. C. Sanders, and A. Lvovsky, Complete characterization of quantum-optical processes, *Science* **322**, 563 (2008).
  - [5] M. Mohseni, A. T. Rezakhani, and D. A. Lidar, Quantum-process tomography: Resource analysis of different strategies, *Phys. Rev. A* **77**, 032322 (2008).
  - [6] A. Keesling et al., Quantum Kibble–Zurek mechanism and critical dynamics on a programmable rydberg simulator, *Nature (London)* **568**, 207 (2019).
  - [7] S. Ebadi et al., Quantum phases of matter on a 256-atom programmable quantum simulator, *Nature (London)* **595**, 227 (2021).
  - [8] S. Chaudhury, S. Merkel, T. Herr, A. Silberfarb, I. H. Deutsch, and P. S. Jessen, Quantum control of the hyperfine spin of a Cs atom ensemble, *Phys. Rev. Lett.* **99**, 163002 (2007).
  - [9] M. Saffman, T. G. Walker, and K. Mølmer, Quantum information with Rydberg atoms, *Rev. Mod. Phys.* **82**, 2313 (2010).
  - [10] E. Ben Av, Y. Shapira, N. Akerman, and R. Ozeri, Direct reconstruction of the quantum-master-equation dynamics of a trapped-ion qubit, *Phys. Rev. A* **101**, 062305 (2020).
  - [11] C. Figgatt, A. Ostrander, N. M. Linke, K. A. Landsman, D. Zhu, D. Maslov, and C. Monroe, Parallel entangling operations on a universal ion-trap quantum computer, *Nature (London)* **572**, 368 (2019).
  - [12] Y. Nam et al., Ground-state energy estimation of the water molecule on a trapped-ion quantum computer, *npj Quantum Inf.* **6**, 33 (2020).
  - [13] M. Howard, J. Twamley, C. Wittmann, T. Gaebel, F. Jelezko, and J. Wrachtrup, Quantum process tomography and Lindblad estimation of a solid-state qubit, *New J. Phys.* **8**, 33 (2006).
  - [14] X.-Q. Zhou, H. Cable, R. Whittaker, P. Shadbolt, J. L. O’Brien, and J. C. Matthews, Quantum-enhanced tomography of unitary processes, *Optica* **2**, 510 (2015).
  - [15] X. Wang, X. Zhan, Y. Li, L. Xiao, G. Zhu, D. Qu, Q. Lin, Y. Yu, and P. Xue, Generalized quantum measurements on a higher-dimensional system via quantum walks, *Phys. Rev. Lett.* **131**, 150803 (2023).
  - [16] Q. Wang, D. Lyu, J. Liu, and J. Wang, Polarization and orbital angular momentum encoded quantum toffoli gate enabled by diffractive neural networks, *Phys. Rev. Lett.* **133**, 140601 (2024).
  - [17] F. Arute et al., Quantum supremacy using a programmable superconducting processor, *Nature (London)* **574**, 505 (2019).
  - [18] G. O. Samach et al., Lindblad tomography of a superconducting quantum processor, *Phys. Rev. Appl.* **18**, 064056 (2022).
  - [19] R. T. Thew, K. Nemoto, A. G. White, and W. J. Munro, Qudit quantum-state tomography, *Phys. Rev. A* **66**, 012303 (2002).
  - [20] Y. Wang, Z. Hu, B. C. Sanders, and S. Kais, Qudits and high-dimensional quantum computing, *Front. Phys.* **8**, 589504 (2020).
  - [21] A. Klimov, R. Guzmán, J. Retamal, and C. Saavedra, Qutrit quantum computer with trapped ions, *Phys. Rev. A* **67**, 062313 (2003).
  - [22] G. D’Ariano and P. L. Presti, Quantum tomography for measuring experimentally the matrix elements of an arbitrary quantum operation, *Phys. Rev. Lett.* **86**, 4195 (2001).
  - [23] G. A. White, F. A. Pollock, L. C. Hollenberg, K. Modi, and C. D. Hill, Non-Markovian quantum process tomography, *PRX Quantum* **3**, 020344 (2022).
  - [24] F. Di Colandrea, N. Dehghan, A. D’Errico, and E. Karimi, Fourier quantum process tomography, *npj Quantum Inf.* **10**, 49 (2024).
  - [25] V. Bužek, Reconstruction of Liouvillian superoperators, *Phys. Rev. A* **58**, 1723 (1998).
  - [26] P. Hayden and J. Sorce, A canonical Hamiltonian for open quantum systems, *J. Phys. A: Math. Theor.* **55**, 225302 (2022).
  - [27] R. Finkelstein, S. Bali, O. Firstenberg, and I. Novikova, A practical guide to electromagnetically induced transparency in atomic vapor, *New J. Phys.* **25**, 035001 (2023).
  - [28] S. Li, P. Dai, J. Liu, Z. Xu, and K. Chida, Spin relaxation of rubidium atoms in an octadecyltrichlorosilane anti-relaxation and anti-reflection coated vacuum multipass cell, *Opt. Mater. Express* **12**, 4384 (2022).
  - [29] G. Lindblad, On the generators of quantum dynamical semigroups, *Commun. Math. Phys.* **48**, 119 (1976).
  - [30] V. Gorini, A. Kossakowski, and E. C. G. Sudarshan, Completely positive dynamical semigroups of n-level systems, *J. Math. Phys.* **17**, 821 (1976).
  - [31] F. Bloch, Generalized theory of relaxation, *Phys. Rev.* **105**, 1206 (1957).
  - [32] A. G. Redfield, On the theory of relaxation processes, *IBM J. Res. Dev.* **1**, 19 (1957).
  - [33] E. B. Davies, Markovian master equations, *Commun. Math. Phys.* **39**, 91 (1974).
  - [34] U. Singh, A. Sawicki, and J. K. Korbicz, Pointer states in the born-markov approximation, *Phys. Rev. Lett.* **132**, 030203 (2024).
  - [35] C.-D. Han, B. Glaz, M. Haile, and Y.-C. Lai, Tomography of time-dependent quantum hamiltonians with machine learning, *Phys. Rev. A* **104**, 062404 (2021).
  - [36] K. Siva et al., Time-dependent hamiltonian reconstruction using continuous weak measurements, *PRX Quantum* **4**, 040324 (2023).
  - [37] D. Aguiar, K. Wold, S. Denisov, and P. Ribeiro, Quantum liouvillian tomography, *arXiv preprint arXiv:2504.10393* (2025).
  - [38] R. A. Bertlmann and P. Krammer, Bloch vectors for qudits, *J. Phys. A: Math. Theor.* **41**, 235303 (2008).
  - [39] G. Benenti and G. Strini, Simple representation of quantum process tomography, *Phys. Rev. A* **80**, 022318 (2009).
  - [40] I. L. Chuang and M. A. Nielsen, Prescription for experimental determination of the dynamics of a quantum black box, *J. Mod. Opt.* **44**, 2455 (1997).
  - [41] J. Poyatos, J. I. Cirac, and P. Zoller, Complete characterization of a quantum process: the two-bit quantum gate, *Phys. Rev. Lett.* **78**, 390 (1997).
  - [42] M. Kopciuch, M. Smolis, A. Miranowicz, and S. Pustelny, Optimized optical tomography of quantum states of a room-temperature alkali-metal vapor, *Phys. Rev. A* **109**, 032402 (2024).
  - [43] A. Dezhang Fard, M. Kopciuch, Y. Sun, P. Włodarczyk, and S. Pustelny, Isolating pure quadratic Zeeman splitting, *Phys. Rev. Appl.* **23**, 064034 (2025).
  - [44] S. Pustelny, V. Schultze, T. Scholtes, and D. Budker,

- Dichroic atomic vapor laser lock with multi-gigahertz stabilization range, *Rev. Sci. Instrum.* **87** (2016).
- [45] Supplementary information for quantum process tomography of a room-temperature alkali-metal vapor.
  - [46] J. Du, X. Rong, N. Zhao, Y. Wang, J. Yang, and R. Liu, Preserving electron spin coherence in solids by optimal dynamical decoupling, *Nature (London)* **461**, 1265 (2009).
  - [47] S. Abo, P. Tulewicz, K. Bartkiewicz, Ş. K. Özdemir, and A. Miranowicz, Experimental Liouvillian exceptional points in a quantum system without Hamiltonian singularities, *New J. Phys.* **26**, 123032 (2024).
  - [48] N. Boulant, T. F. Havel, M. A. Pravia, and D. G. Cory, Robust method for estimating the Lindblad operators of a dissipative quantum process from measurements of the density operator at multiple time points, *Phys. Rev. A* **67**, 042322 (2003).
  - [49] L. Zhang, A. Datta, H. B. Coldenstrodt-Ronge, X.-M. Jin, J. Eisert, M. B. Plenio, and I. A. Walmsley, Recursive quantum detector tomography, *New J. Phys.* **14**, 115005 (2012).
  - [50] A. Anis and A. Lvovsky, Maximum-likelihood coherent-state quantum process tomography, *New J. Phys.* **14**, 105021 (2012).
  - [51] D. Mogilevtsev, J. Řeháček, and Z. Hradil, Self-calibration for self-consistent tomography, *New J. Phys.* **14**, 095001 (2012).
  - [52] S. T. Merkel, J. M. Gambetta, J. A. Smolin, S. Poletto, A. D. Córcoles, B. R. Johnson, C. A. Ryan, and M. Steffen, Self-consistent quantum process tomography, *Phys. Rev. A* **87**, 062119 (2013).
  - [53] F. Minganti, A. Miranowicz, R. W. Chhajlany, and F. Nori, Quantum exceptional points of non-Hermitian Hamiltonians and Liouvillians: The effects of quantum jumps, *Phys. Rev. A* **100**, 062131 (2019).
  - [54] M. Kopciuch and A. Miranowicz, Liouvillian and Hamiltonian exceptional points of atomic vapors: The spectral signatures of quantum jumps, *arXiv preprint arXiv:2506.02902* (2025).
  - [55] A. Rivas, S. A. Huelga, and M. B. Plenio, Quantum non-markovianity: characterization, quantification and detection, *Rep. Prog. Phys.* **77**, 094001 (2014).
  - [56] T. Luan, Z. Li, C. Zheng, X. Kuang, X. Yu, and Z. Zhang, Non-Markovian Quantum Process Tomography, *Symmetry* **16**, 180 (2024).
  - [57] A. Browaeys and T. Lahaye, Many-body physics with individually controlled Rydberg atoms, *Nat. Phys.* **16**, 132 (2020).
  - [58] R. Blatt and C. Roos, Quantum simulations with trapped ions, *Nat. Phys.* **8**, 277 (2012).
  - [59] H. Torlai et al., Neural-network quantum state tomography, *Nat. Phys.* **14**, 447 (2018).
  - [60] X. t. Zhang, Learning and forecasting open quantum dynamics with correlated noise, *Commun. Phys.* **8**, 29 (2025).
  - [61] M. Bukov et al., Reinforcement learning in different phases of quantum control, *Phys. Rev. X* **8**, 031086 (2018).
  - [62] M. Y. Niu et al., Universal quantum control through deep reinforcement learning, *npj Quantum Inf.* **5**, 33 (2019).
  - [63] J. Schlienz and G. Mahler, Description of entanglement, *Phys. Rev. A* **52**, 4396 (1995).

# Supplementary Information for Quantum Process Tomography of a Room-Temperature Alkali-Metal Vapor

Yujie Sun

*Marian Smoluchowski Institute of Physics, Jagiellonian  
University in Kraków, 30-348 Kraków, Poland*

Marek Kopciuch\*

*Institute of Spintronics and Quantum Information, Faculty of  
Physics, Adam Mickiewicz University, 61-614 Poznań, Poland and  
Marian Smoluchowski Institute of Physics, Jagiellonian  
University in Kraków, 30-348 Kraków, Poland*

Arash Dezhang Fard

*Marian Smoluchowski Institute of Physics, Jagiellonian  
University in Kraków, 30-348 Kraków, Poland and  
Doctoral School of Exact and Natural Sciences,  
Jagiellonian University in Kraków, 30-348 Kraków, Poland*

Szymon Pustelny<sup>†</sup>

*Marian Smoluchowski Institute of Physics, Jagiellonian  
University in Kraków, 30-348 Kraków, Poland and  
Department of Physics, Harvard University, Cambridge, MA 02138, USA*

(Dated: August 28, 2025)

## I. QUANTUM-STATE VECTORIZATION IN THE BLOCH-FANO REPRESENTATION

The density matrix  $\hat{\rho}$ , describing a quantum system with  $d$  energy levels, can be written using the Bloch–Fano representation [1, 2]

$$\hat{\rho} = \frac{1}{d} \hat{\mathbb{1}}_d + \sum_{i=1}^{d^2-1} a_i \hat{\sigma}_i = \sum_{i=1}^{d^2} a_i \hat{\sigma}_i, \quad (\text{S1})$$

where  $\hat{\sigma}_i$  for  $i \in \{1, \dots, d^2 - 1\}$  are the generalized Pauli matrices, which are the  $\text{SU}(d)$  generators, and the operator  $\hat{\sigma}_{d^2} = \sqrt{2/d} \hat{\mathbb{1}}_d$ , with  $\hat{\mathbb{1}}_d$  being the  $d$ -dimensional identity matrix, was introduced to express the expansion in a compact form, with the scaling factor chosen to preserve the simple orthogonality relation for generalized Pauli matrices:

$$\frac{1}{2} \text{Tr}[\hat{\sigma}_i \hat{\sigma}_j] = \delta_{ij}. \quad (\text{S2})$$

This allows us to write the density matrix in a simple vectorized form:

$$\hat{\rho} = \sum_{i=1}^{d^2} \frac{1}{2} \text{Tr}(\hat{\rho} \hat{\sigma}_i) \hat{\sigma}_i = \sum_{i=1}^{d^2} \rho_i \hat{\sigma}_i = |\rho\rangle\rangle \iff |\rho\rangle\rangle_i = \frac{1}{2} \text{Tr}(\hat{\rho} \hat{\sigma}_i), \quad (\text{S3})$$

where the coefficient  $\rho_i$  is a state vector component, representing the projection of the density matrix onto the standard form  $\hat{\sigma}_i$ . These coefficients are real-valued, with the final coefficient constrained by the trace conservation condition  $\rho_{d^2} = \sqrt{1/(2d)}$ . In short, a general density matrix  $\hat{\rho}$  can be written as a vector  $|\rho\rangle\rangle$  in the Bloch–Fano representation.

Since our experimental system of interest is a qutrit, realized in the ground state of total angular momentum  $f = 1$  of the  $^{87}\text{Rb}$  atom, the state is described in a 3-dimensional Hilbert space, where the generalized Pauli matrices are the Gell–Mann matrices ( $\text{SU}(3)$  generators),

---

\* marek.kopciuch@amu.edu.pl

† szymon.pustelny@uj.edu.pl

and the  $\hat{\sigma}_9$  matrix is introduced as described above:

$$\begin{aligned}
\hat{\sigma}_1 &= \begin{pmatrix} 0 & 1 & 0 \\ 1 & 0 & 0 \\ 0 & 0 & 0 \end{pmatrix} & \hat{\sigma}_2 &= \begin{pmatrix} 0 & -i & 0 \\ i & 0 & 0 \\ 0 & 0 & 0 \end{pmatrix} & \hat{\sigma}_3 &= \begin{pmatrix} 1 & 0 & 0 \\ 0 & -1 & 0 \\ 0 & 0 & 0 \end{pmatrix} \\
\hat{\sigma}_4 &= \begin{pmatrix} 0 & 0 & 1 \\ 0 & 0 & 0 \\ 1 & 0 & 0 \end{pmatrix} & \hat{\sigma}_5 &= \begin{pmatrix} 0 & 0 & -i \\ 0 & 0 & 0 \\ i & 0 & 0 \end{pmatrix} & \hat{\sigma}_6 &= \begin{pmatrix} 0 & 0 & 0 \\ 0 & 0 & 1 \\ 0 & 1 & 0 \end{pmatrix} \\
\hat{\sigma}_7 &= \begin{pmatrix} 0 & 0 & 0 \\ 0 & 0 & -i \\ 0 & i & 0 \end{pmatrix} & \hat{\sigma}_8 &= \frac{1}{\sqrt{3}} \begin{pmatrix} 1 & 0 & 0 \\ 0 & 1 & 0 \\ 0 & 0 & -2 \end{pmatrix} & \hat{\sigma}_9 &= \sqrt{\frac{2}{3}} \begin{pmatrix} 1 & 0 & 0 \\ 0 & 1 & 0 \\ 0 & 0 & 1 \end{pmatrix}
\end{aligned} \tag{S4}$$

In this case  $|\rho\rangle\rangle$  is a 9-dimensional state vector, and the process matrix  $\hat{\hat{P}}$ , which accounts for the evolution of the atomic system, is a  $9 \times 9$  real matrix.

## II. QUANTUM STATE TOMOGRAPHY OF A QUTRIT SYSTEM

Quantum State Tomography (QST) is a technique used to reconstruct the density matrix of a quantum state by performing a series of measurements on multiple copies of the state, which is essential for characterizing and verifying quantum states in our experiment. The QST technique used in this paper is described in detail in Ref. [3]. Here, we provide a brief overview.

When a linearly polarized optical beam propagates through an atomic vapor at room temperature, its polarization state undergoes measurable modifications, including changes in ellipticity, phase shift, and optical absorption. These alterations arise from light-matter interactions governed by the atomic susceptibility tensor. Crucially, if the atomic system exhibits time-dependent quantum dynamics, the resulting perturbations imprint the system's underlying properties—such as coherences, populations, and relaxation rates—onto the probe beam's Stokes parameters. Specifically, in the absence of additional external perturbations, the atomic system undergoes intrinsic relaxation processes, leading to the gradual decay of the observed signal amplitude. This time-dependent signal attenuation is

characteristic of free-induction decay (FID).

By detecting the FID signals produced by the atomic ensemble, we access the time-resolved evolution of atomic coherences. Leveraging a complete set of polarization rotation measurements enables us to extract the element-wise correlations within the atomic density matrix. As shown in Ref. [3], the relation between the time( $t$ )- and detuning( $\Delta v$ )-dependent polarization rotation  $\delta\alpha$  and operators  $\hat{\alpha}_{R,I}$  and  $\hat{\beta}$  is given by

$$\delta\alpha(t; \Delta v) = \eta(\Delta v) \left( e^{-\gamma_1 t} [\langle \hat{\alpha}_R \rangle \sin(2\Omega_L t) + \langle \hat{\alpha}_I \rangle \cos(2\Omega_L t)] - \zeta(\Delta v) e^{-\gamma_2 t} \langle \hat{\beta} \rangle \right) \quad (\text{S5})$$

where  $\eta(\Delta v)$  and  $\zeta(\Delta v)$  are the global and local scaling factors, respectively; the operators  $\hat{\alpha}_{R,I}$  and  $\hat{\beta}$  are associated with the coherences and population difference of specific magnetic sublevels. For our system, probed on the transition  $f = 1 \rightarrow F = 2$ , these operators can take the form:

$$\begin{aligned} \hat{\alpha}_R &= \frac{1}{30} (|-1\rangle \langle 1| + |1\rangle \langle -1|), \\ \hat{\alpha}_I &= \frac{i}{30} (|-1\rangle \langle 1| - |1\rangle \langle -1|), \\ \hat{\beta} &= \frac{1}{6} (|-1\rangle \langle -1| - |1\rangle \langle 1|). \end{aligned} \quad (\text{S6})$$

Moreover, polarization rotation  $\delta\alpha$  is also determined by the Larmor frequency  $\Omega_L$  and the longitudinal and transverse relaxation rates  $\gamma_1$  and  $\gamma_2$ . To minimize technical noise and systematic errors caused by uncontrollable phase delays, we adopt the cyclically ordered phase sequence (CYCLOPS) method (for more information, see Ref. [3]) to detect the FID signal.

Figure 1(a) and (b) show the experimentally measured polarization rotations (blue dots) and the corresponding theoretical fits (red lines), obtained via a CYCLOPS measurement for a qutrit polarized along the  $x$ -axis. Through the analysis of the fitting results, we quantitatively determine the expectation values of the operators  $\hat{\alpha}_R$ ,  $\hat{\alpha}_I$ , and  $\hat{\beta}$ , which provide partial information about the system.

A single measurement is insufficient due to the limited information it provides on the density matrix elements, therefore, we must perform additional measurements by applying rotations to the atomic ensemble to achieve complete quantum state tomography of a qutrit system. Specifically, we apply geometrical rotation of the state around the  $x$ - and  $y$ -axes using  $\pi/2$  pulses, thereby transforming the measured observables. These measurements provide linearly independent constraints on the density matrix elements, resolving the

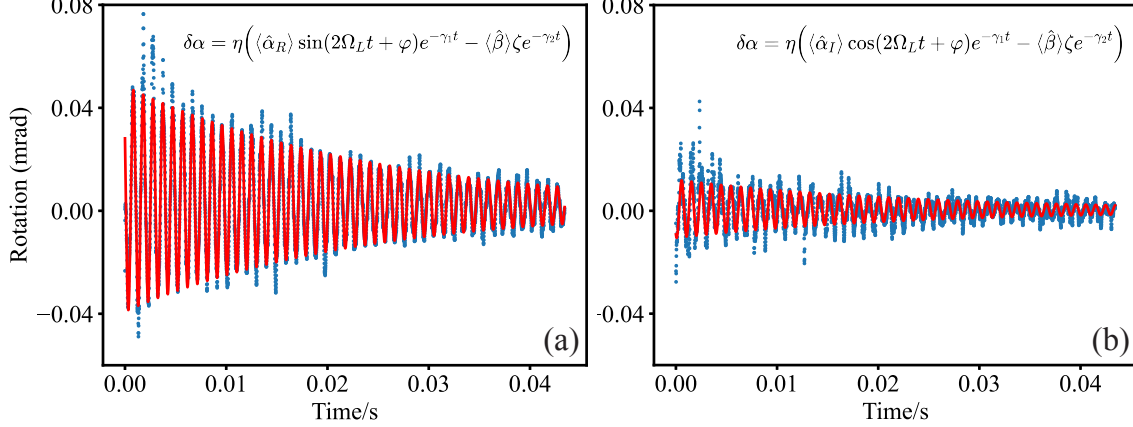


FIG. 1. Detected polarization rotations (blue dots) and fitted dependences (red lines) by using a CYCLOPS measurement for a qutrit state with maximal stretch along the  $x$ -axis. (a) Estimation of the population difference  $\langle\hat{\beta}\rangle = 4.26 \times 10^{-3}$  and the real part of coherence  $\langle\hat{\alpha}_R\rangle = 1.56 \times 10^{-2}$ . (b) Estimation of the population difference  $\langle\hat{\beta}\rangle = 7.12 \times 10^{-4}$  and the imaginary part of coherence  $\langle\hat{\alpha}_I\rangle = -4.03 \times 10^{-3}$ .

remaining degrees of freedom. Finally, we employ a linear inversion method to reconstruct the full density matrix  $\hat{\rho}$  by solving the system of equations derived from the combined measurements.

### III. QUANTUM PROCESS TOMOGRAPHY — DISSIPATOR RECONSTRUCTION

As mentioned in the main text, the core idea of process estimation is to compare a set of initial states with their counterparts after undergoing the measured process. For complete QPT characterization, we prepare an informationally complete set of initial states spanning the Hilbert space of a qutrit system. This set consists of  $N = 15$  linearly independent states, constructed as eigenstates of the Gell-Mann matrices:

$$|\psi_k\rangle = \begin{cases} |i\rangle \\ \frac{1}{\sqrt{2}} (|i\rangle + e^{i\phi} |j\rangle) \end{cases} \quad (\text{S7})$$

where  $i, j \in \{-1, 0, 1\}$  index the qutrit levels, and  $\phi \in \{0, \pi/2, \pi, 3\pi/2\}$  ensures phase diversity. Table I presents these theoretical initial states and the corresponding experimental realizations ( $\hat{\rho}_k$ ) obtained via optimized magnetic-field pulse sequences (combining strong

oscillating and weak static fields), measured using the QPT technique described in Sec. II. These experimentally prepared states  $\hat{\rho}_k$  form the columns of the input-state matrix  $\mathbb{M}^{(i)}$ , as defined in the main text, which serves as the basis for further evolution and analysis.

Each prepared quantum state subsequently undergoes unitary and non-unitary evolution under the influence of the target environment. The resulting time-evolved states  $\hat{\rho}'_k$  are experimentally reconstructed using QST (see Sec. II), forming the output-state matrix  $\mathbb{M}^{(o)}$ . In the Bloch-Fano representation, the evolution is described by:

$$\mathbb{M}^{(o)} = \hat{\hat{P}}(t)\mathbb{M}^{(i)}. \quad (\text{S8})$$

To address the overcompleteness of the input state set ( $N = 15 > d^2 = 9$ ), we define symmetrized input- and output-state matrices as:

$$\underline{\mathbb{M}}^{(i,o)} = \mathbb{M}^{(i,o)} \cdot (\mathbb{M}^{(i)})^\dagger, \quad (\text{S9})$$

which enables the reconstruction of the process matrix through linear inversion of the symmetrized form of Eq. (S8):

$$\hat{\hat{P}}(t) = \underline{\mathbb{M}}^{(o)} \left( \underline{\mathbb{M}}^{(i)} \right)^{-1}. \quad (\text{S10})$$

This method enables the estimation of the process matrix  $\hat{\hat{P}}(t)$  at different evolution times. Figure 2 shows examples of experimentally measured process matrices in the Bloch-Fano representation, capturing system dynamics driven solely by the effective total relaxation superoperator  $\hat{\hat{R}}_T$ , as discussed in the main text. Ideally, the elements of the process matrix lie within the interval  $[-1, 1]$ ; however, experimental imperfections such as statistical noise, systematic errors, and reconstruction inaccuracies, can cause deviations from this range.

Moreover, the set of measured process matrices, such as those presented in Fig. 2, allows for the reconstruction of the dissipator  $\hat{\hat{R}}_T$  using Eq. (14) from the main text. The resulting dissipator is shown in Fig. 3(a).

To gain further insight into the underlying relaxation mechanisms, we model  $\hat{\hat{R}}_T$  as a sum of three distinct processes:

1. Isotropic relaxation typical for paraffin-coated atomic-vapor cells, represented by  $\hat{\hat{R}}_{\text{iso}} = \mathbb{1}_9 - \delta_{99}$ , where the last diagonal element remains zero to ensure trace preservation.

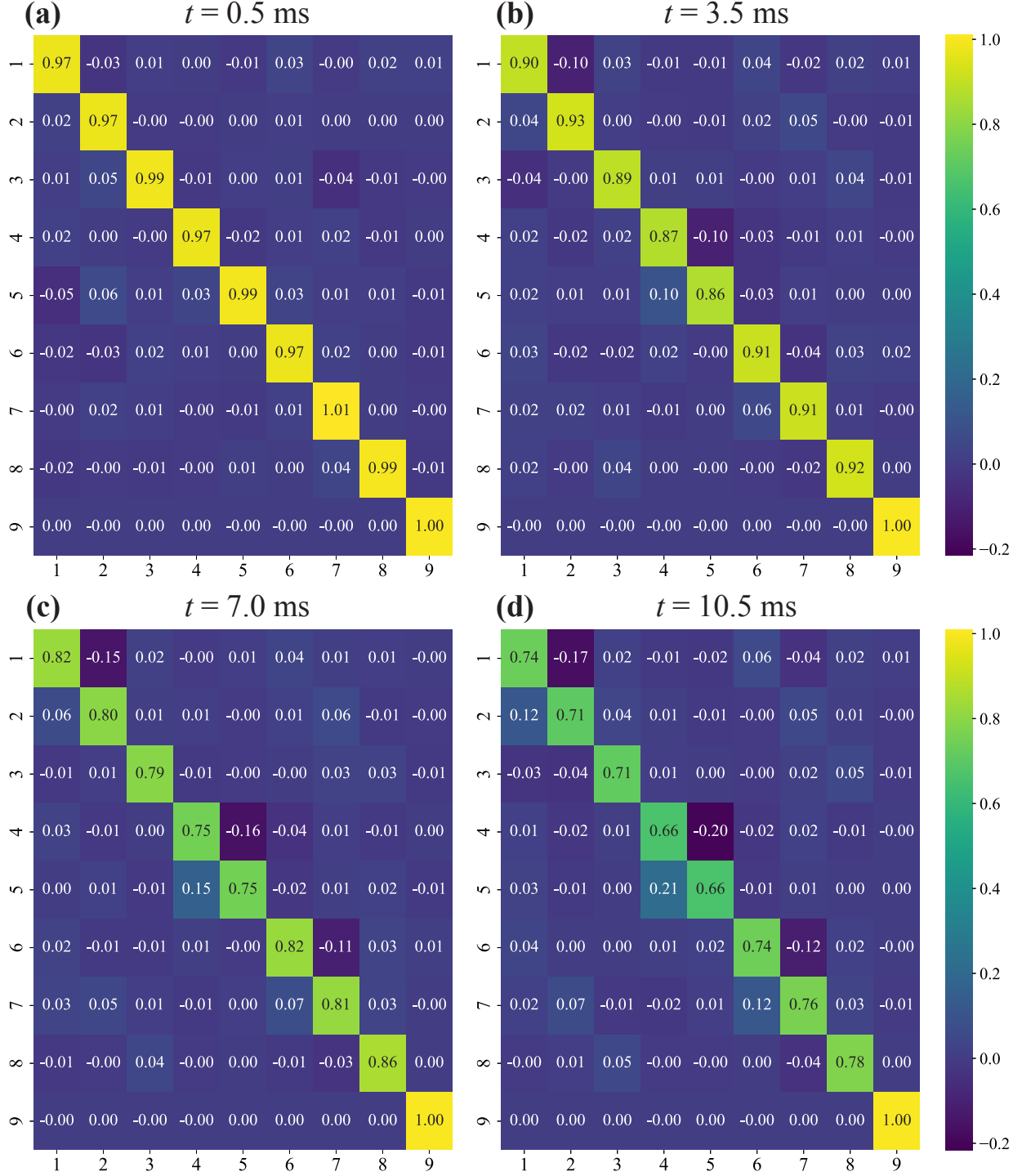


FIG. 2. Examples of experimentally measured process matrices  $\hat{P}(t)$  at different evolution times under the action of the effective total relaxation superoperator  $\hat{R}_T$ .

2. Relaxation due to residual magnetic fields, modeled by a Hamiltonian  $\hat{H}_k = (\mathbf{\Omega}_L)_k \hat{F}_k$ .

3. Dephasing, modeled analogously to the qubit case, using three independent Lindblad operators  $\hat{L}_k = \gamma_k \hat{F}_k$ .

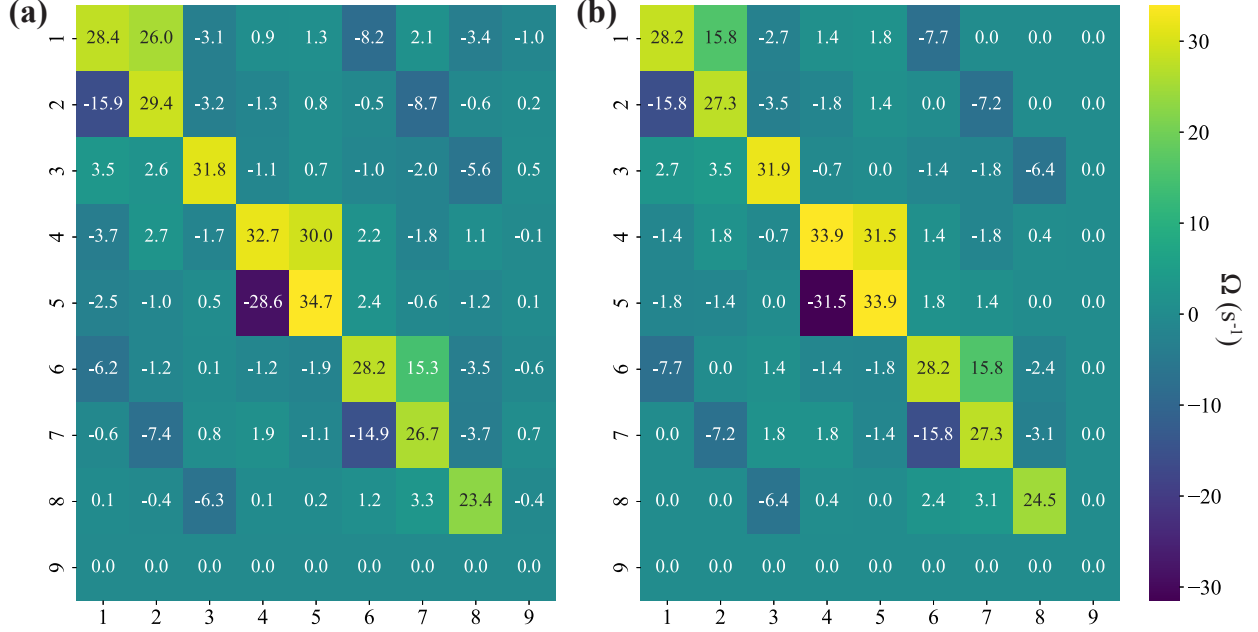


FIG. 3. (a) Reconstruction of the effective total relaxation superoperator  $\hat{\hat{R}}_T$  using the MLE protocol. (b) Estimated relaxation superoperator described using a model including isotropic relaxation, residual magnetic fields, and magnetic field gradients.

From the measured  $\hat{\hat{R}}_T$  shown in Fig. 3(a), and using the described model, we estimate the residual Larmor frequencies as  $\Omega_L/2\pi = \{-0.397^{+0.011}_{-0.011}, 0.3071^{+0.0091}_{-0.0091}, 2.511^{+0.034}_{-0.034}\}$  Hz, the dephasing rates as  $\gamma_k = \{7.0^{+1.0}_{-1.0}, 7.9^{+1.1}_{-1.1}, 6.6^{+1.3}_{-1.3}\} \text{ s}^{-1}$ , and the isotropic relaxation rate as  $\gamma_i = 13.3^{+1.6}_{-1.6} \text{ s}^{-1}$ .

#### IV. RECONSTRUCTION OF STATIC MAGNETIC FIELDS

As a systematic supplementary validation of our time-independent Hamiltonian reconstruction, we characterize the reconstruction of the Hamiltonian caused by linear Zeeman splitting. Figures 4(a-c) visually demonstrate the Hamiltonian comparison between theoretical predictions, direct reconstruction, and MLE along the  $x$ -,  $y$ -, and  $z$ -axes, respectively. Quantitative analysis shows that the relative errors between the theoretical Hamiltonian superoperator and the reconstruction via MLE are  $0.01835^{+0.00037}_{-0.00037}$ ,  $0.0219^{+0.0011}_{-0.0011}$ , and

$0.02853^{+0.00015}_{-0.00015}$ , while those for direct reconstruction are  $0.0186^{+0.0023}_{-0.0023}$ ,  $0.0212^{+0.0019}_{-0.0019}$ , and  $0.04389^{+0.0018}_{-0.0018}$ , respectively. Figure 4(d) presents a quantitative relative error analysis comparing the process matrices  $\hat{\hat{P}}$  generated by the Hamiltonian using direct reconstruction and MLE with the experimental measurements when the static magnetic field is applied along three orthogonal axes ( $x$ ,  $y$ , and  $z$ ), respectively. All relative errors are bounded by  $0.158^{+0.065}_{-0.065}$ . Notably, there is excellent agreement between reconstructions via both methods and predictions under static magnetic field conditions, which verifies the reliability of the experimental system and confirms the accuracy of the Hamiltonian reconstruction method.

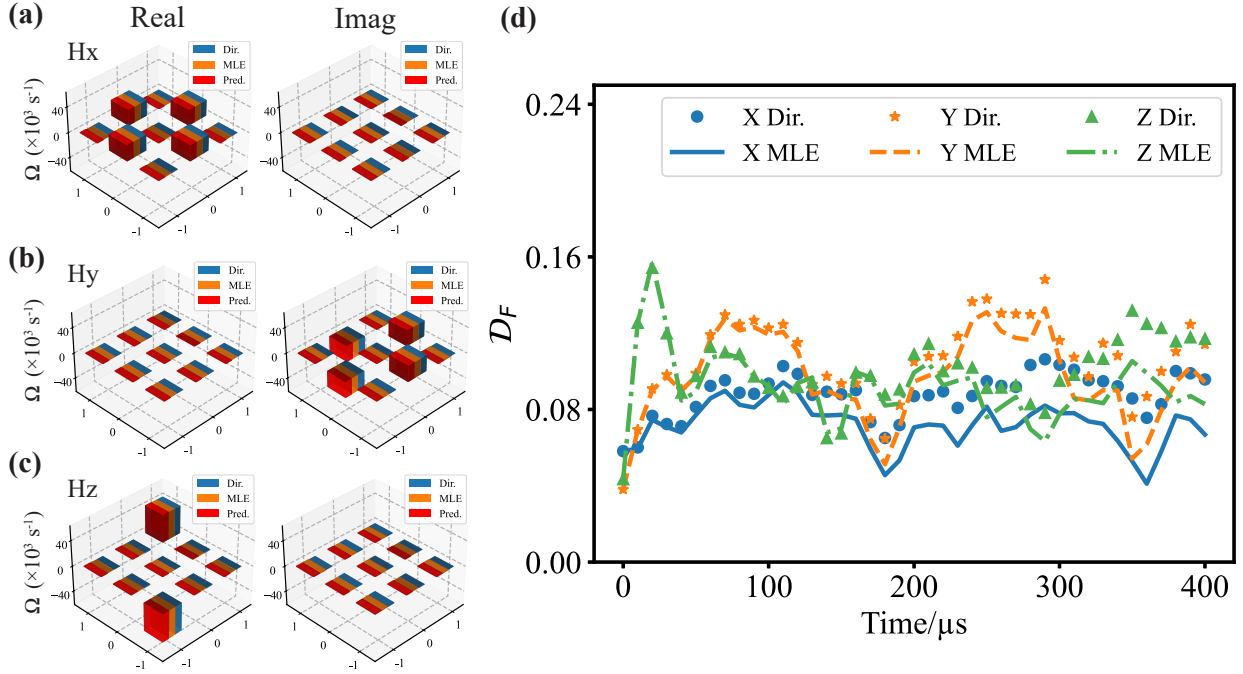


FIG. 4. (a-c) Comparison of the Hamiltonian operators. When the magnetic field is aligned along the  $x$ -,  $y$ -, and  $z$ -axes, the relative error via MLE is  $\mathcal{D}_F = 0.01835^{+0.00037}_{-0.00037}$ ,  $0.0219^{+0.0011}_{-0.0011}$ ,  $0.02853^{+0.00015}_{-0.00015}$  respectively, while for direct reconstruction it is  $\mathcal{D}_F = 0.0186^{+0.0023}_{-0.0023}$ ,  $0.0212^{+0.0019}_{-0.0019}$ ,  $0.0439^{+0.0018}_{-0.0018}$  respectively. (d) Normalized Frobenius distance between the experimentally measured process superoperators and those generated from the estimated  $\hat{\hat{H}}_C$  using direct reconstruction (points) and MLE (lines) when the static magnetic field is along the  $x$ -,  $y$ -, and  $z$ -axes.

TABLE I: Initial states: Theory vs. Experiment

States	Theory	Experiment	Fidelity
$\hat{\rho}_1$	$\begin{pmatrix} 1 & 0 & 0 \\ 0 & 0 & 0 \\ 0 & 0 & 0 \end{pmatrix}$	$\begin{pmatrix} 0.919 & 0.001 - 0.080i & 0.011 + 0.011i \\ 0.001 + 0.080i & 0.045 & -0.012 - 0.017i \\ 0.011 - 0.011i & -0.012 + 0.017i & 0.036 \end{pmatrix}$	0.919
$\hat{\rho}_2$	$\begin{pmatrix} 0 & 0 & 0 \\ 0 & 1 & 0 \\ 0 & 0 & 0 \end{pmatrix}$	$\begin{pmatrix} 0.069 & -0.017 + 0.039i & -0.018 - 0.001i \\ -0.017 - 0.039i & 0.878 & 0.004 + 0.007i \\ -0.018 + 0.001i & 0.004 - 0.007i & 0.053 \end{pmatrix}$	0.878
$\hat{\rho}_3$	$\begin{pmatrix} 0 & 0 & 0 \\ 0 & 0 & 0 \\ 0 & 0 & 1 \end{pmatrix}$	$\begin{pmatrix} 0.036 & 0.011 + 0.015i & 0.007 - 0.027i \\ 0.011 - 0.015i & 0.072 & -0.038i \\ 0.007 + 0.027i & 0.038i & 0.892 \end{pmatrix}$	0.892
$\hat{\rho}_4$	$\begin{pmatrix} 0.5 & 0.5 & 0 \\ 0.5 & 0.5 & 0 \\ 0 & 0 & 0 \end{pmatrix}$	$\begin{pmatrix} 0.460 & 0.423 - 0.018i & 0.020 - 0.030i \\ 0.423 + 0.018i & 0.478 & 0.044 - 0.077i \\ 0.020 + 0.030i & 0.044 + 0.077i & 0.062 \end{pmatrix}$	0.892
$\hat{\rho}_5$	$\begin{pmatrix} 0.5 & -0.5i & 0 \\ 0.5i & 0.5 & 0 \\ 0 & 0 & 0 \end{pmatrix}$	$\begin{pmatrix} 0.467 & 0.041 - 0.436i & -0.010 + 0.021i \\ 0.041 + 0.436i & 0.480 & -0.035 - 0.033i \\ -0.010 - 0.021i & -0.035 + 0.033i & 0.053 \end{pmatrix}$	0.909
$\hat{\rho}_6$	$\begin{pmatrix} 0.5 & -0.5 & 0 \\ -0.5 & 0.5 & 0 \\ 0 & 0 & 0 \end{pmatrix}$	$\begin{pmatrix} 0.473 & -0.437 - 0.092i & 0.047 - 0.026i \\ -0.437 + 0.092i & 0.514 & -0.043 + 0.045i \\ 0.047 + 0.026i & -0.043 - 0.045i & 0.013 \end{pmatrix}$	0.931
$\hat{\rho}_7$	$\begin{pmatrix} 0.5 & 0.5i & 0 \\ -0.5i & 0.5 & 0 \\ 0 & 0 & 0 \end{pmatrix}$	$\begin{pmatrix} 0.472 & -0.144 + 0.402i & -0.053 + 0.036i \\ -0.144 - 0.402i & 0.487 & 0.023 + 0.021i \\ -0.053 - 0.036i & 0.023 - 0.021i & 0.041 \end{pmatrix}$	0.882

Table I continued

States	Theory	Experiment	Fidelity
$\hat{\rho}_8$	$\begin{pmatrix} 0 & 0 & 0 \\ 0 & 0.5 & 0.5 \\ 0 & 0.5 & 0.5 \end{pmatrix}$	$\begin{pmatrix} 0.034 & 0.066 + 0.011i & 0.042 - 0.031i \\ 0.066 - 0.011i & 0.532 & 0.410 - 0.075i \\ 0.042 + 0.031i & 0.410 + 0.075i & 0.434 \end{pmatrix}$	0.893
$\hat{\rho}_9$	$\begin{pmatrix} 0 & 0 & 0 \\ 0 & 0.5 & -0.5i \\ 0 & 0.5i & 0.5 \end{pmatrix}$	$\begin{pmatrix} 0.041 & 0.025 - 0.052i & -0.047 + 0.008i \\ 0.025 + 0.052i & 0.544 & -0.033 - 0.421i \\ -0.047 - 0.008i & -0.033 + 0.421i & 0.415 \end{pmatrix}$	0.901
$\hat{\rho}_{10}$	$\begin{pmatrix} 0 & 0 & 0 \\ 0 & 0.5 & -0.5 \\ 0 & -0.5 & 0.5 \end{pmatrix}$	$\begin{pmatrix} 0.054 & -0.066 - 0.019i & 0.027 + 0.005i \\ -0.066 + 0.019i & 0.513 & -0.408 + 0.006i \\ 0.027 - 0.005i & -0.408 - 0.006i & 0.433 \end{pmatrix}$	0.881
$\hat{\rho}_{11}$	$\begin{pmatrix} 0 & 0 & 0 \\ 0 & 0.5 & 0.5i \\ 0 & -0.5i & 0.5 \end{pmatrix}$	$\begin{pmatrix} 0.057 & -0.049 + 0.068i & -0.022 + 0.005i \\ -0.049 - 0.068i & 0.527 & -0.038 + 0.419i \\ -0.022 - 0.005i & -0.038 - 0.419i & 0.416 \end{pmatrix}$	0.890
$\hat{\rho}_{12}$	$\begin{pmatrix} 0.5 & 0 & 0.5 \\ 0 & 0 & 0 \\ 0.5 & 0 & 0.5 \end{pmatrix}$	$\begin{pmatrix} 0.523 & -0.016 - 0.010i & 0.415 - 0.002i \\ -0.016 + 0.010i & 0.037 & -0.007 - 0.002i \\ 0.415 + 0.002i & -0.007 + 0.002i & 0.440 \end{pmatrix}$	0.897
$\hat{\rho}_{13}$	$\begin{pmatrix} 0.5 & 0 & -0.5i \\ 0 & 0 & 0 \\ 0.5i & 0 & 0.5 \end{pmatrix}$	$\begin{pmatrix} 0.540 & -0.041 - 0.010i & 0.063 - 0.435i \\ -0.040 + 0.010i & 0.036 & 0.021 + 0.025i \\ 0.063 + 0.435i & 0.021 - 0.025i & 0.424 \end{pmatrix}$	0.917
$\hat{\rho}_{14}$	$\begin{pmatrix} 0.5 & 0 & -0.5 \\ 0 & 0 & 0 \\ -0.5 & 0 & 0.5 \end{pmatrix}$	$\begin{pmatrix} 0.540 & -0.005 + 0.013i & -0.397 - 0.070i \\ -0.005 - 0.013i & 0.025 & 0.012 + 0.007i \\ -0.397 + 0.070i & 0.012 - 0.007i & 0.435 \end{pmatrix}$	0.885

Table I continued

States	Theory	Experiment	Fidelity
$\hat{\rho}_{15}$	$\begin{pmatrix} 0.5 & 0 & 0.5i \\ 0 & 0 & 0 \\ -0.5i & 0 & 0.5 \end{pmatrix}$	$\begin{pmatrix} 0.525 & 0.019 + 0.022i & -0.134 + 0.404i \\ 0.019 - 0.022i & 0.044 & 0.004 - 0.006i \\ -0.134 - 0.404i & 0.004 + 0.006i & 0.431 \end{pmatrix}$	0.882

- 
- [1] R. A. Bertlmann and P. Krammer, Bloch vectors for qudits, J. Phys. A: Math. Theor. **41**, 235303 (2008).
- [2] G. Benenti and G. Strini, Simple representation of quantum process tomography, Phys. Rev. A **80**, 022318 (2009).
- [3] M. Kopciuch, M. Smolis, A. Miranowicz, and S. Pustelny, Optimized optical tomography of quantum states of a room-temperature alkali-metal vapor, Phys. Rev. A **109**, 032402 (2024).